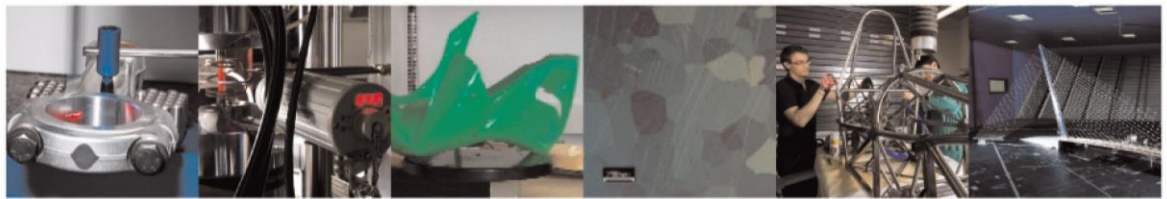




POLITECNICO
MILANO 1863

DIPARTIMENTO DI MECCANICA



Mechanistic force model for double-phased high-feed mills

Bernini L.; Albertelli P.; Monno M.

This is a post-peer-review, pre-copyedit version of an article published in INTERNATIONAL JOURNAL OF MECHANICAL SCIENCES. The final authenticated version is available online at: <http://dx.doi.org/10.1016/j.ijmecsci.2022.107801>

This content is provided under [CC BY-NC-ND 4.0](https://creativecommons.org/licenses/by-nc-nd/4.0/) license



Mechanistic force model for double-phased high-feed mills

L Bernini^{a,b,*}, P Albertelli^{a,b} and M Monno^{a,b}

^aDepartment of Mechanical Engineering, Politecnico di Milano, via La Masa 1, 20156 Milan, Italy.

^bMUSP Macchine Utensili Sistemi di Produzione, strada della Torre della Razza, 29122 Piacenza, Italy.

ARTICLE INFO

Keywords:

High-feed milling
Double-phased cutters
Specific force coefficients
Analytical mechanistic model
Mean cutting forces
Mean cutting torque and power

ABSTRACT


Being able to predict cutting forces, torque and power in machining applications allows to check their influence on the quality of the product, to assess the feasibility of the process and to compare different operations for sustainability purposes. In this paper, the analytical development of a mechanistic model for cutting forces prediction for high-feed mills is carried out. High-feed cutters are featured by extremely low lead angles, leading to a gradual engagement of the cutter inside the workpiece. This fact prevents the mechanistic literature formulation to accurately compute the undeformed instantaneous chip section of each cutter, and thus to correctly predict the spindle torque and power. A closed analytical formulation for the mechanistic cutting force model, including an improved chip thickness formulation with variable entry and exit angles and double-phased cutter geometry, is presented. Experimental cutting tests using double-phased high-feed mills were carried out on Ti_6Al_4V with variable feed rate per tooth, cutting speed and axial depth of cut. The model was assessed by comparing the performances of the literature model and the developed high-feed one in the identification of specific force coefficients - SFC. The identified SFC resulted to belong to two statistically different populations. SFC 95% confidence intervals were found to be significantly narrower with respect to the literature ones. K_{tc} 95% confidence intervals were equal to (1085; 1426) MPa and (970; 2423) MPa for the proposed and literature model, respectively. The validity of the proposed model was assessed in terms of mean forces, mean spindle torque and mean spindle power prediction capabilities. The Root Mean Squared Prediction Error for the proposed model resulted to be remarkably lower (15 N , 0.33 Nm , 29 W) with respect to literature model (41 N , 1.25 Nm , 120 W).

Nomenclature

Abbreviations

AD	Anderson-Darling
AICc	Corrected Akaike information criterion
ANOVA	Analysis of variance
BIC	Bayesian information criterion
CI	Confidence intervals
CL	Altintas literature model
DF	Degrees of freedom
FEM	Finite Element Method
HF	High-feed model
MAPE	Mean absolute percentage error
MS	Mean squares
PI	Prediction intervals
PRESS	Predicted residual error sum of squares
QQ Normality Plot	Quantiles-quantiles normality plot

*Corresponding author

 luca1.bernini@polimi.it (L. Bernini);

paolo.albertelli@polimi.it (P. Albertelli); michele.monno@polimi.it (M. Monno)

ORCID(s): 0000-0002-7064-7518 (L. Bernini); 0000-0001-5098-0420 (P. Albertelli); 0000-0002-1957-3613 (M. Monno)

RMSPE Root mean squared prediction error

SFC Specific force coefficients

SS Sum of squares

Symbols

α	Significance level
$\beta_k, \hat{\beta}_k$	"True" and estimated SFC for model k
Σ_{β_k}	Covariance matrix of SFC for model k
χ	Lead angle
$\hat{P}_{CL}, \hat{P}_{HF}$	Predicted mean power through model CL or HF
$\hat{T}_{CL}, \hat{T}_{HF}$	Predicted mean torque through model CL or HF
$\mathbf{a}_{q,k}$	Vector to transform SFC in quantity q (mean torque or power) using model k
\mathbf{C}_k	Inverse of the Gram matrix
\mathbf{e}_k	Estimated residuals of model k
\mathbf{X}_k	Design matrix for model k
$\mathbf{x}_{0,k}$	Regression vector for a new observation for model k
$\mathbf{y}, \hat{\mathbf{y}}$	Measured mean forces and predicted responses (mean forces components) through model k
$\mathcal{N}(\cdot)$	Normal distribution

\bar{F}	Mean force	$r_{A,j}^*, r_{l,j}^*$	Radial coordinates of undeformed chip area and edge contact length centres of mass
$\sigma_k^2, \hat{\sigma}_k^2$	"True" and estimated residual variance for model k	r_1, r_2, r_3, r_4	High-feed cutter geometrical vertices radial coordinates
$\varepsilon_{m,k}$	Residual term of test m for model k	r_φ	Segment connecting the actual centre of the mill to the workpiece end
φ	Cutter angular position	$r_{a,ext}, r_{a,int}$	Radial distances of current and previous profile intersections with axial depth of cut line
φ_0	Initial phase of first cutter	r_{nom}	High-feed mill nominal radius
$\varphi_{a,ext}, \varphi_{a,int}$	Axial depth of cut engagement critical angles	$s_{q,k}^2$	Predicted quantity q (mean torque or power) variance using model k
$\varphi_{i,ext}, \varphi_{i,int}$	Engagement critical angles	T	Cutting torque
$\varphi_{st}, \varphi_{ex}$	Entry and exit angles	t	Time
A, l	Chip area and edge contact length	T_P	Mill revolution period
a	Axial depth of cut	$t_{\cdot,\cdot}$	t-Student distribution
a_{do}	Constants for mean forces components	v_c	Cutting speed
A_{int}, A_{ext}	Chip area under previous and current cutter profiles	$x_{do,k}$	Regressor for o-th SFC on d-th mean force component for model k
b	Radial depth of cut	y_0	True response for a new observation
c	Feed per tooth	z	Axial reference frame coordinate
D	Mill diameter	z_1, z_2, z_3, z_4	High-feed cutter geometrical vertices axial coordinates
d	Direction index	z_{ext}, z_{int}	High-feed current and previous cutter profile functions in z-r plane.
F_t, F_r, F_a	Tangential, radial and axial cutting force components		
F_x, F_y, F_z	x, y and z cutting force components		
g	Engagement function		
h	Instantaneous chip thickness		
i	High-feed cutter geometrical vertex index		
j	Cutter index		
k	Model index (either CL or HF)		
$K_{t,c}, K_{r,c}, K_{a,c}$	Tangential, radial and axial cutting SFC		
$K_{t,e}, K_{r,e}, K_{a,e}$	Tangential, radial and axial edge SFC		
M	Number of tests		
m	Observation index		
N	Number of mill cutters		
n	Rotational speed		
n_p	Number of observations		
o	Regressor index		
P	Cutting power		
p	Number of predictors		
r	Radial reference frame coordinate		

1. Introduction

Milling is a flexible chip removal process that allows for the production of several kind of goods such as aeronautical and biomedical ones [1]. The capability of predicting the forces acting on the tool is of fundamental importance. In fact, cutting forces influence on the milling operation is twofold: on one hand, they are representative of the performances of the operation; on the other hand, they allow for the estimation of related quantities, such as torque and power [2], that are needed to check the feasibility of the milling operation on the available machine [3], as well as to compare multiple operations in a sustainability perspective. Cutting forces are the cause for machine tool vibrations, that can be either forced [4], being responsible for reduced workpiece surface quality and geometrical accuracy, or regenerative [5], mining the process stability [6, 7, 8, 9]. Indeed, cutting force models are the main sources of information and mathematical tools for stability analysis [10, 11, 12] and even chip formation mechanism determination [13]. Furthermore, within the Industry 4.0 paradigm, cutting forces and related quantities can be used to predict

the remaining useful life of the milling tool [6, 14, 15, 16]. Being able to predict cutting forces beforehand, allows to compare them with nominal ones. At last, cutting forces are the main source of information to analyse the energetic behaviour of a process in terms of specific cutting energies, which represent the main focus of this paper.

In literature, force prediction models in milling applications are grouped in three main categories: physical models, numerical models and mechanistic models. The first category tries to link the cutting forces to the mechanical properties of the material and the geometrical configuration of the cut. Representative of this category is the famous work by Merchant [17]. In opposition to such methods, numerical approaches try to predict the cutting forces by studying the interaction between the tool and the workpiece [3]. In between the above categories, mechanistic models try to fuse the physical and empirical worlds. They relate cutting forces to geometrical quantities involved in the cutting process through empirical coefficients that need to be identified (specific force coefficients, SFC). In literature, there are two well established formulations: exponential models and linear models. Exponential models consider cutting forces as an exponential function of the average chip area. Models of this kind can be found in [18, 19, 20]. Linear models divide the cutting forces into two contributions instead. The first one is directly linked to the shearing action on the shear plane and friction on the rake face of the tool and it is proportional to the undeformed chip cross-sectional area by a specific cutting energy or cutting pressure. The second contribution is represented by the ploughing actions under the flank face of the cutter on the workpiece. This term is proportional to the cutting edge length through the edge SFC [21].

In literature, several works dealt with mechanistic modelling of different kind of mills: square shoulder mills, which feature the simplest geometry, and end mills. Square shoulder mills were the reference case for the Altintas model [21]. Research deeply analysed this kind of mills proposing several upgrades to the Altintas theory. More specifically, the main improvements on the Altintas model regarded the geometrical properties of the trajectory of the mill and its cutters. In fact, the original theory was based on some important assumptions: the cycloidal trajectory of each tooth does not allow for a closed solution for the chip thickness, which was approximated through a sinusoidal function of the feed per tooth, then. A second assumption regarded the cutter run-out: teeth were considered evenly spaced and featured by the same radius. These assumptions brought Wan *et al.* [22], firstly, Kumanchick and Schmitz [23], secondly, and Matsumura and Tumura [24], lastly, to propose extensions of the model, even considering different cutter geometries, e.g. end-mills. Cutting forces were decomposed in a nominal contribution and a run-out contribution (that vanishes in the coefficients identification); cycloidal motion of the mill teeth was introduced with higher order approximations, improving both the accuracy of the chip thickness formulation and the tooth path description. In [25] and [26],

helical flute geometry was introduced, considering the helix angle in order to move from orthogonal cutting SFC to oblique cutting context; furthermore, more general tool geometries were considered, i.e. ball, ball nose, taper and ball taper mills. With [27], tool wear started to be included in mechanistic formulations of cutting forces. Actual chip-tool contact area and rubbing forces were included in the prediction of cutting forces. Later, Zhu and Zhang proposed a tool wear model with adjustable coefficients. Once included in the mechanistic formulation, prediction of cutting forces reached a 98.5% agreement with experimental instantaneous cutting forces [28]. Zhang *et al.* proposed a model that took into consideration teeth trochoidal trajectories, run-out and tool wear [29]. Even textured tools were analysed [30], where thin shear zone theory and unified cutting mechanics allowed to predict a reduction in the cutting thrust force. In order to compensate cutting forces measurements, inverse-based filtering with the inclusion of a mechanistic model considering workpiece deflection was introduced in [31]. With the objective of assessing cutting operation stability, structural dynamics of both tool and workpiece, and tool orientation were included in the analysis [32]. Sahoo *et al.* proposed a hybrid mechanistic approach, considering trochoidal tool trajectory, tool run-out, minimum chip thickness and all preceding teeth trajectories; SFC were extracted from FEM simulations [33]. Modification of mechanistic models were found even in exotic applications, like turn-milling [34], or like bone milling, where it was possible to include osteon orientation, tool geometry and edge effect with unified mechanics approach. Furthermore, heat flux was used to model surface temperature, too [35]. Some other improvements were proposed in the framework of micro-milling. Edge radius and material strengthening effects, together with overlapping tooth engagements, were firstly introduced [36]. Li *et al.* proposed a general undeformed chip thickness model accounting for trochoidal trajectory, tool run-out and the material removed by multiple preceding teeth [37]. Later, radius size-effect, tool deflection, variable entry and exit angles and minimum uncut chip thickness were added to the model [38]. Li and Wu presented cutting coefficients as functions of the instantaneous chip thickness, estimating them from FEM simulations [39], while Zhou *et al.* included the elastic recovery of the material in the uncut chip thickness formulation [40]. Run-out, tilt offset and tooth trajectory were integrated in the cutting force model by Zhang *et al.*, considering a distributed load on the tool to predict its deflection [41]. Jing *et al.* proposed a formulation including variable entry and exit angles, minimum chip thickness, tool run-out and elastic recovery. The mechanistic model assumed a hybrid fashion, estimating SFC through FEM simulations. They found that elastic recovery plays an important role only at low feed rates [42]. Wan *et al.* investigated the effects of uncut chip thickness on the shearing and ploughing force components. They proposed a formulation based on a combination of plastic formation theory and slip-line field theory, allowing to compute the shape of the dead metal zone [43]. More recently, the inclusion of

cutters run-out, radius size-effect and variable entry and exit angles were also proposed for average uncut chip thickness formulations [44]. Zhou *et al.* introduced wear-varying cutting edge with non-linear associated behaviours, i.e. non-linear tool-chip friction and strain gradient plasticity effects, in order to estimate the shear flow stress [45]. Even the numerical computation of curved chip thickness models was introduced, capable of mimicking the chip flow on the rake face of the cutting insert [46]. At last, Kilic and Altintas proposed a generalization of mechanics and dynamics of metal cutting operations, capable of simulating operations such as turning, milling, boring and drilling, while accounting for general cutter geometries, run-out and tool-workpiece relative vibrations [47, 48].

Altintas model allowed also for the identification of the proportionality coefficients. The coefficient estimations are typically performed through multivariate linear regression models on the average forces [49]. Different works recently dealt with the identification of the SFC of mechanistic models from various cutting tests based on the extensions of the model [1, 50, 51]. Guo *et al.* provided a mathematical formulation for the mechanistic model of a five-axis ball-end mill together with the identification method for the model coefficients [52]. Gonzalo *et al.* proposed an instantaneous approach to fit the SFC for end-mills. They compared the identified coefficients with those obtained from orthogonal turning tests with the average identification procedure. Identified SFC resulted to be in accordance with those from orthogonal turning tests, providing a better physical description of cutting forces with variable chip thickness [3].

The design procedure of machining processes conducts to an optimisation problem. Typically, in order to obtain the lowest cutting times, the function to be optimised is the material removal rate. It depends on the axial depth of cut, the radial depth of cut and the feed rate. The analysis of machine tool vibrations identified the axial depth of cut as the main source of instability, namely chatter instability [53, 21, 54]. This discovery led tool manufacturers towards newer directions for the maximisation of the material removal rate. Indeed, they started to develop more complicated geometries for the cutters. Such tools are known as high-feed mills. High-feed mills rely on chip thinning in order to reach higher feed per tooth values. Their geometrical characteristics allow for a reduced radial load on the spindle, while generating higher axial forces during the cut. Researchers address cutters as "high-feed" when they can achieve up to ten times the feed rate and three times the material removal rate compared with conventional mills [55]. Such cutters may reach feed per tooth over mill radius ratios ranging from 0.03 up to 0.4 [56, 57, 58, 55, 59, 60, 61]. This capability was obtained through the use of really low lead angles and, more specifically, using double-phased cutters, i.e. cutters featured by two consecutive sections with different lead angles.

Literature analysis revealed absence, to the best of authors knowledge, of mechanistic modelling of high-feed mills. Furthermore, the improvements related to cycloidal trajectory of the tooth were relevant and appreciable for mills with

a really high feed per tooth over mill diameter ratio, i.e. for micro-milling operations and not for high-feed milling, where this ratio is still considerably lower [23]. All the other improvements allowed for a better representation of the uncut chip thickness, and thus, to better cutting force predictions. Anyway, they all introduced complex geometrical and mathematical formulations that needed numerical approaches based on discretization (e.g. [46]) or time integration ([47, 48]), leading to slow computational operations. On the contrary, the conceived approach is completely analytical and in closed form, allowing for the exact solution of the equations with fast computational times, while keeping high prediction capabilities and outperforming literature analytical approaches. The developed model considers the variable entry and exit angles, while parametrically considering high-feed cutter geometries. At last, the conceived model allows for the identification of SFC based on average cutting forces. In this paper, the analytical formulation of the mechanistic model for high-feed mills (that will be consistently indicated as HF) is introduced, while the differences with respect to the classical Altintas model (CL) will be analysed. In section 2 the HF model is presented, providing the main analytical formulas of the model. The mean fitting procedure is described, showing the construction procedure of the design matrix. The design of experiments is then explained together with the performed statistical analysis, including model fitting and uncertainty propagation on validation quantities. In section 3, the whole regression analysis output is furnished and its in-depth discussion is performed. In section 4, the novelties and contributions of the work are highlighted. At the end of the paper, the theoretical background is included in appendix A, with the equations related to the CL model. Two appendixes, B and C, describe the proof of the instantaneous and mean forces derivations, respectively.

2. Materials and methods

In this section, the whole work procedure was described following the order of figure 1. The HF model development is firstly presented, highlighting formulation differences with respect to the CL model (appendix A). Then, the experimental set-up and the experimental campaign are introduced. The methods for the identification of the SFC and the validation analysis will conclude this section.

2.1. High-feed analytical model

The development of the HF model is presented in this section (fig. 1C-D). High-feed mills are featured by double-phased low lead angles cutters, as can be seen in figure 2a. The mill nominal radius is r_{nom} , while the number of cutters is N . The machining process is featured by the feed per tooth c and the rotational speed n . The formulation starts by defining the position in time of the cutters [51] through equation 1:

$$\varphi_j(t) = \varphi_0 + \frac{2\pi(j-1)}{N} + 2\pi n t \quad (1)$$

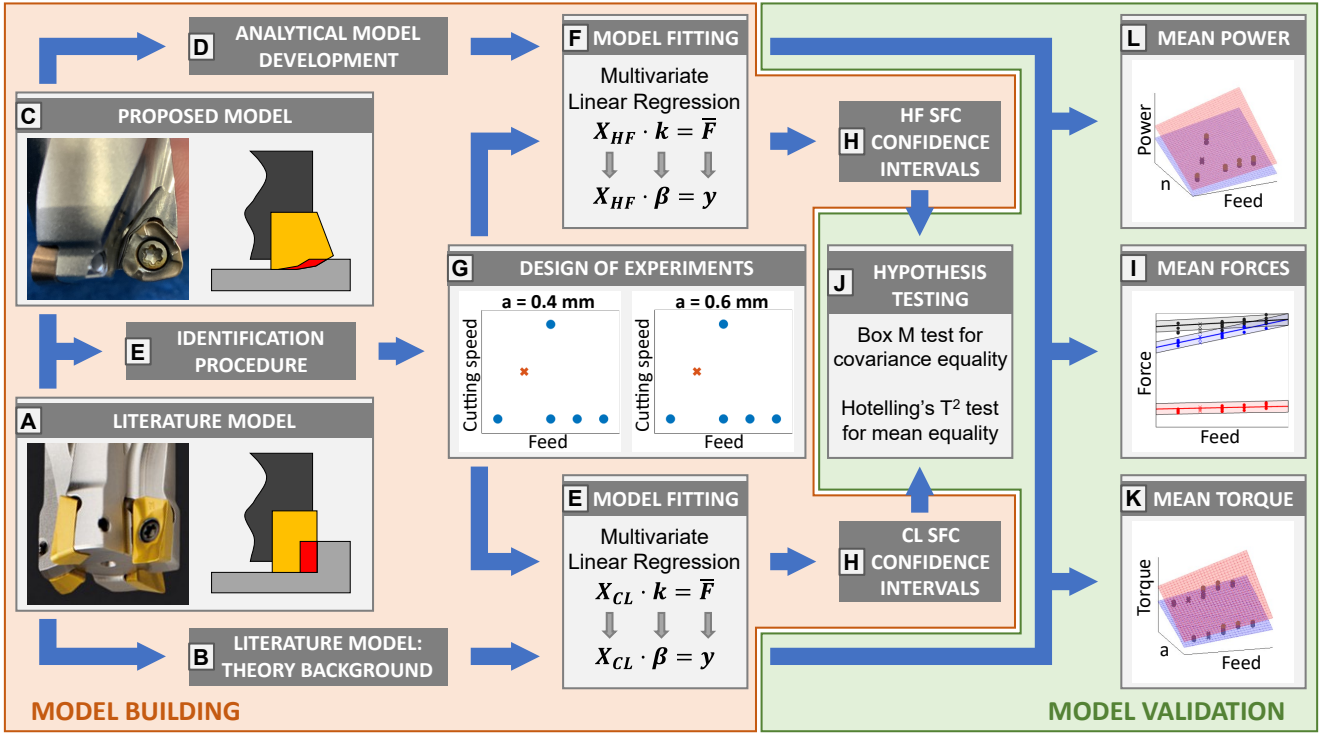


Figure 1: Graphical representation of the developed work. From left to right: literature (A) and high-feed (C) mill cutters; reference (B) and proposed (D) analytical formulations allow to estimate SFC through a Multivariate Linear Regression Problem (E-F); the estimation is performed by cutting tests, designed to vary feed per tooth, cutting speed and axial depth of cut (G); the estimated SFC and their confidence intervals are compared in terms of mean and variance through multivariate hypothesis tests (H-J); the proposed model is validated and compared with the literature model through the prediction of mean forces (I), torque (K) and power (L).

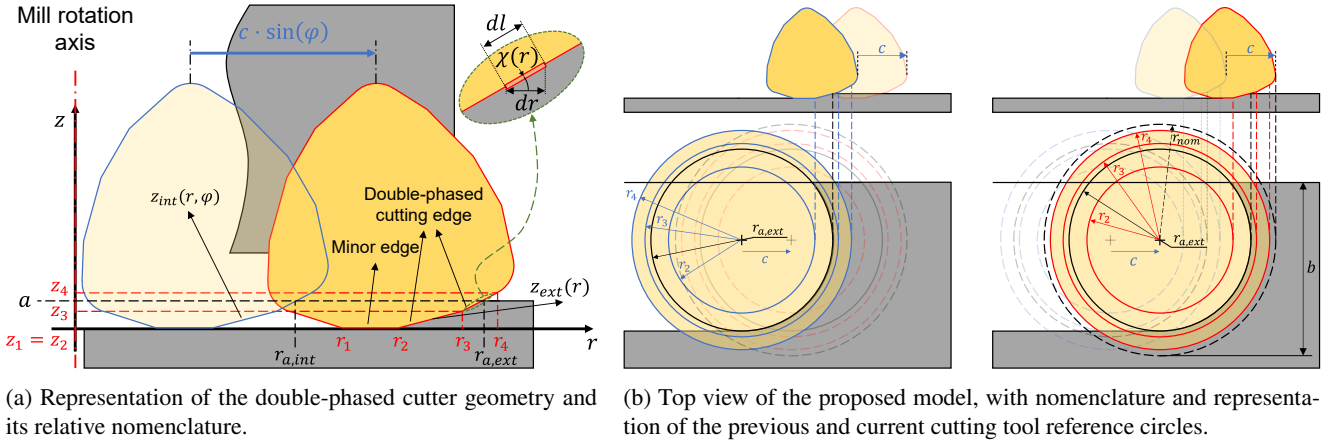


Figure 2: High-feed model reference figure. The cutting insert profile is shown relatively to the previous cutter position for a generic cutter angle φ . Each vertex of the double-phased cutting edge can be projected on the top view, and can be seen as the associated circle of radius r_i .

where t is the time; $j = 1, 2, \dots, N$ denotes the j -th cutter; φ_0 is the angular position of cutter 1 at $t = 0$. The dependence on time of the cutter angles will be omitted in the following. The instantaneous chip thickness removed by cutter j is approximated by equation 2:

$$h(\varphi_j) = c \sin \varphi_j \quad (2)$$

For the next steps, it is necessary to make reference to figures 2a and 2b for the cutter geometry description.

Looking at the plane $z - r$ that passes through the mill axis at the current position and the radius at given φ angle from the y -axis (fig. 2a), the cutter profile coordinates in actual and previous position (z_{ext} and z_{int} , respectively), are defined as functions of the radial coordinate r from the mill

actual axis of rotation:

$$z_{ext}(r) = \begin{cases} 0, & \text{if } r_1 \leq r \leq r_2 \\ \frac{z_3}{r_3-r_2} (r-r_2), & \text{if } r_2 < r \leq r_3 \\ z_3 + \frac{z_4-z_3}{r_4-r_3} (r-r_3), & \text{if } r_3 < r \leq r_4 \end{cases} \quad (3)$$

$$z_{int}(r, \varphi) = \begin{cases} \frac{z_3}{r_3-r_2} [r-r_2+h(\varphi)], & \text{if } r_2-h(\varphi) < r \leq r_3-h(\varphi) \\ z_3 + \frac{z_4-z_3}{r_4-r_3} [r-r_3+h(\varphi)], & \text{if } r_3-h(\varphi) < r \leq r_4-h(\varphi) \\ z_4, & \text{if } r_4-h(\varphi) < r \leq r_4 \end{cases} \quad (4)$$

where r_i and z_i , with $i = 2, 3, 4$ are shown in figure 2a and $z_1 = z_2 = 0$; the j index was omitted for simplicity. As can be seen from equations 3 and 4, high-feed mills present a radial extension of the cutter profile. This feature implies that φ_{st} is a function of the axial coordinate z (fig. 3a-3b). The developed model, in opposition to the CL model, takes into account this effect. First of all, the radial depth of cut b is defined with respect to the nominal radius of the mill r_{nom} (this is done to match what an operator does practically). A reference circle associated to each particular radius (i.e. r_i and $i = 1, 2, 3, 4$) can be drawn in the reference model (figure 2b). It is possible to determine different critical angles, computed with respect to the y-axis, at which the radius of each circle ends on the edge of the workpiece (eq. 5):

$$\begin{aligned} \varphi_{i,ext} &= \arccos \frac{b-r_{nom}}{r_i}, \quad i = 2, 3, 4 \\ \varphi_{i,int} &= \arctan \frac{r_i \sin \varphi_{i,ext} - c}{b-r_{nom}}, \quad i = 2, 3, 4 \end{aligned} \quad (5)$$

Such angles determine the transition regions from an undeformed chip shape to a different shape (due to the engagement of a different section of the cutter profile, fig. 3a-3b). The possibility to introduce transition regions in the mathematical formulation of the model represents a difference with respect to the CL model. The axial depth of cut introduces the last two critical angles, at which the cutter profile is engaged at its maximum height. It is necessary to introduce the radii of intersection between the external and internal cutter profiles with the axial depth of cut line (eq. 6):

$$\begin{aligned} r_{a,ext} &= \begin{cases} r_2 + \frac{r_3-r_2}{z_3} a, & \text{if } a \leq z_3 \\ r_3 + \frac{r_4-r_3}{z_4-z_3} (a-z_3), & \text{if } a > z_3 \end{cases} \\ r_{a,int}(\varphi) &= r_{a,ext} - h(\varphi) \end{aligned} \quad (6)$$

It must be pointed out that $r_{a,int}(\varphi)$ is not a radius, but just the radial distance between the actual mill centre and the intersection of the previous cutter profile with the axial depth

of cut line. It is then possible to compute the critical angles associated to $r_{a,ext}$ and $r_{a,int}(\varphi)$ (eq. 7):

$$\begin{aligned} \varphi_{a,ext} &= \arccos \frac{b-r_{nom}}{r_{a,ext}} \\ \varphi_{a,int} &= \arctan \frac{r_{a,ext} \sin \varphi_{a,ext} - c}{b-r_{nom}} \end{aligned} \quad (7)$$

At this point, the area and the edge contact length differentials can be defined by equation 8:

$$\begin{aligned} dA(r) &= [z_{int}(r) - z_{ext}(r)] dr = \\ &= dA_{int}(r) - dA_{ext}(r) \\ dl(r) &= \frac{dr}{\cos \chi(r)} \end{aligned} \quad (8)$$

where $\chi(r)$ is the lead angle at the current r radial coordinate.

The three components of the cutting forces (i.e. tangential, radial and axial) acting on cutter j are expressed in differential form (eq. 9):

$$\begin{aligned} dF_{t,j}(\varphi_j) &= K_{t,c} dA(\varphi_j) + K_{t,e} dl(\varphi_j) \\ dF_{r,j}(\varphi_j) &= K_{r,c} dA(\varphi_j) + K_{r,e} dl(\varphi_j) \\ dF_{a,j}(\varphi_j) &= K_{a,c} dA(\varphi_j) + K_{a,e} dl(\varphi_j) \end{aligned} \quad (9)$$

where $K_{d,c}$ and $K_{d,e}$, with $d = t, r, a$, are the cutting and edge specific force coefficients (SFC), respectively. The first ones account for the shearing action on the shear plane and the friction effect on the rake face of the cutting edge, whereas the edge SFC are related to the ploughing action under the flank face of the cutting edge [51].

Substituting equation 8 in equation 9 and integrating it in the radial direction, leads to the expression of the instantaneous forces. The integration bounds are equal to $r_2 - h(\varphi)$ and $r_\varphi(\varphi)$, that is the length of the segment connecting the actual centre of the mill to the workpiece end (eq. 10):

$$r_\varphi(\varphi) = \begin{cases} \frac{b-r_{nom}}{\cos \varphi}, & \text{if } \varphi \leq \varphi_{a,ext} \\ r_{a,ext}, & \text{if } \varphi > \varphi_{a,ext} \end{cases} \quad (10)$$

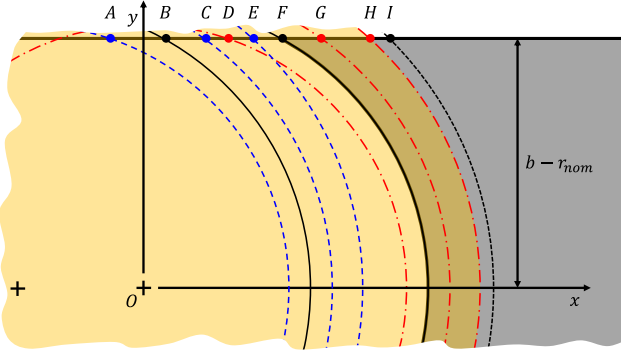
Since the engagement condition was already considered in the differential terms, the instantaneous cutting forces are:

$$\begin{aligned} F_{t,j}(\varphi_j) &= K_{t,c} [A_{int}(\varphi_j) - A_{ext}(\varphi_j)] + K_{t,e} l(\varphi_j) \\ F_{r,j}(\varphi_j) &= K_{r,c} [A_{int}(\varphi_j) - A_{ext}(\varphi_j)] + K_{r,e} l(\varphi_j) \\ F_{a,j}(\varphi_j) &= K_{a,c} [A_{int}(\varphi_j) - A_{ext}(\varphi_j)] + K_{a,e} l(\varphi_j) \end{aligned} \quad (11)$$

The force components are then projected in the feed, normal and axial direction of the milling operation, and the contribution of each cutter is summed up in equation 12:

$$\begin{aligned} F_x(t) &= - \sum_{j=1}^N F_{t,j}(\varphi_j) \cos \varphi_j - \sum_{j=1}^N F_{r,j}(\varphi_j) \sin \varphi_j \\ F_y(t) &= + \sum_{j=1}^N F_{t,j}(\varphi_j) \sin \varphi_j - \sum_{j=1}^N F_{r,j}(\varphi_j) \cos \varphi_j \\ F_z(t) &= + \sum_{j=1}^N F_{a,j}(\varphi_j) \end{aligned} \quad (12)$$

Distances:			Angles:		
\overline{OA} : $r_{2,int}$	\overline{OD} : $r_{2,ext}$	\overline{OG} : $r_{3,ext}$	\widehat{AOy} : $\varphi_{2,int}$	\widehat{DOy} : $\varphi_{2,ext}$	\widehat{GOy} : $\varphi_{3,ext}$
\overline{OB} : $r_{a,int}$	\overline{OE} : $r_{4,int}$	\overline{OH} : $r_{4,ext}$	\widehat{BOy} : $\varphi_{a,int}$	\widehat{EOy} : $\varphi_{4,int}$	\widehat{HOy} : $\varphi_{4,ext}$
\overline{OC} : $r_{3,int}$	\overline{OF} : $r_{a,ext}$	\overline{OI} : r_{nom}	\widehat{COy} : $\varphi_{3,int}$	\widehat{FOy} : $\varphi_{a,ext}$	


 (a) $a \leq z_3$ case.

Distances:			Angles:		
\overline{OA} : $r_{2,int}$	\overline{OD} : $r_{2,ext}$	\overline{OG} : $r_{a,ext}$	\widehat{AOy} : $\varphi_{2,int}$	\widehat{DOy} : $\varphi_{2,ext}$	\widehat{GOy} : $\varphi_{a,ext}$
\overline{OB} : $r_{3,int}$	\overline{OE} : $r_{4,int}$	\overline{OH} : $r_{4,ext}$	\widehat{BOy} : $\varphi_{3,int}$	\widehat{EOy} : $\varphi_{4,int}$	\widehat{HOy} : $\varphi_{4,ext}$
\overline{OC} : $r_{a,int}$	\overline{OF} : $r_{3,ext}$	\overline{OI} : r_{nom}	\widehat{COy} : $\varphi_{a,int}$	\widehat{FOy} : $\varphi_{3,ext}$	

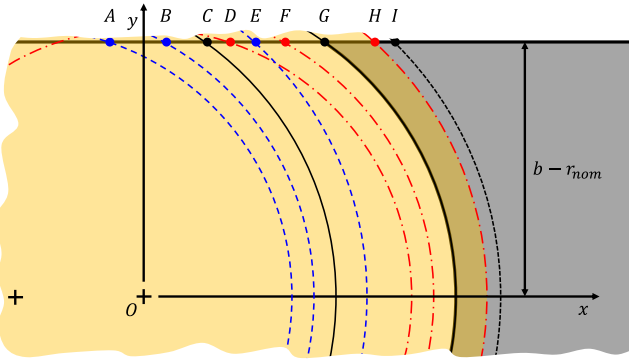
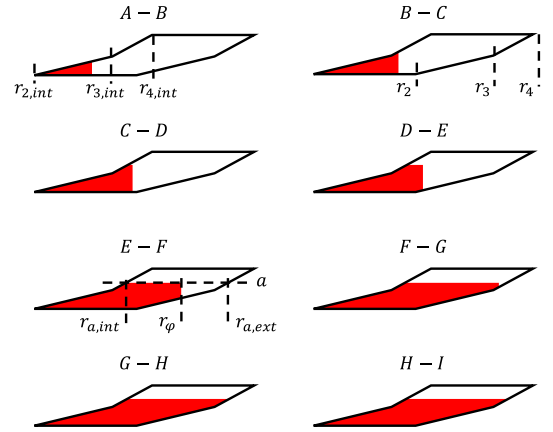
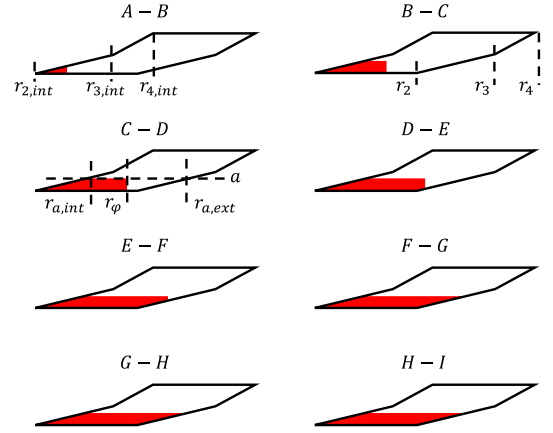

 (b) $a > z_3$ case.


Figure 3: Previous (dashed) and current (dash-dotted) cutting tool reference circles. Circles with solid lines are generated by the axial engagement. The critical angles $\varphi_{i,int}$ and $\varphi_{i,ext}$ determine the regions where the shape of the undeformed chip changes. On the right the chip shapes vary according to the angular position of the tool. A different chip shape is obtained when the tool radius passes between two points (indicated as pairs over the chip shape itself).

Forces are expressed as functions of time since $\varphi_j = \varphi_j(t)$.

In order to identify experimentally the six SFC, a procedure based on mean cutting forces was developed [62, 51]. Equation 11 is then substituted in equation 12 and integrated over one period of revolution T_P of the mill. The resulting expressions for mean forces are reported in equation 13:

$$\begin{aligned} \overline{F}_x &= \frac{N}{2\pi} (-a_{11} K_{t,c} - a_{12} K_{t,e} - a_{13} K_{r,c} - a_{14} K_{r,e}) \\ \overline{F}_y &= \frac{N}{2\pi} (a_{21} K_{t,c} + a_{22} K_{t,e} - a_{23} K_{r,c} - a_{24} K_{r,e}) \\ \overline{F}_z &= \frac{N}{2\pi} (a_{35} K_{a,c} + a_{36} K_{a,e}) \end{aligned} \quad (13)$$

where a_{do} are constant terms depending on the mill geometry, the feed per tooth (c) and the depths of cut (a and b).

The computation of the torque, requires more steps than for the CL model. This is due to the fact that the distance of the infinitesimal tangential force has an increasing arm

with respect to its z coordinate of application. Starting from the infinitesimal tangential force, the associated infinitesimal torque is:

$$dT_j(r) = K_{t,c} r dA_j(r) + K_{t,e} r dl_j(r) \quad (14)$$

By integrating equation 14 over the radial coordinate of the undeformed chip and summing up the contributions of the N cutters, the resulting torque is constituted by two terms:

$$\begin{aligned} T(t) &= \sum_{j=1}^N \left\{ K_{t,c} r_{A,j}^* [A_{int}(\varphi_j) - A_{ext}(\varphi_j)] + \right. \\ &\quad \left. + K_{t,e} r_{l,j}^* l(\varphi_j) \right\} \end{aligned} \quad (15)$$

where $r_{A,j}^*$ and $r_{l,j}^*$ are the radial coordinates of the centre of mass of the undeformed chip area and edge contact length, respectively. The cutting power is computed by substituting equation 15 in equation A.7. Complete expressions for A_{int} ,

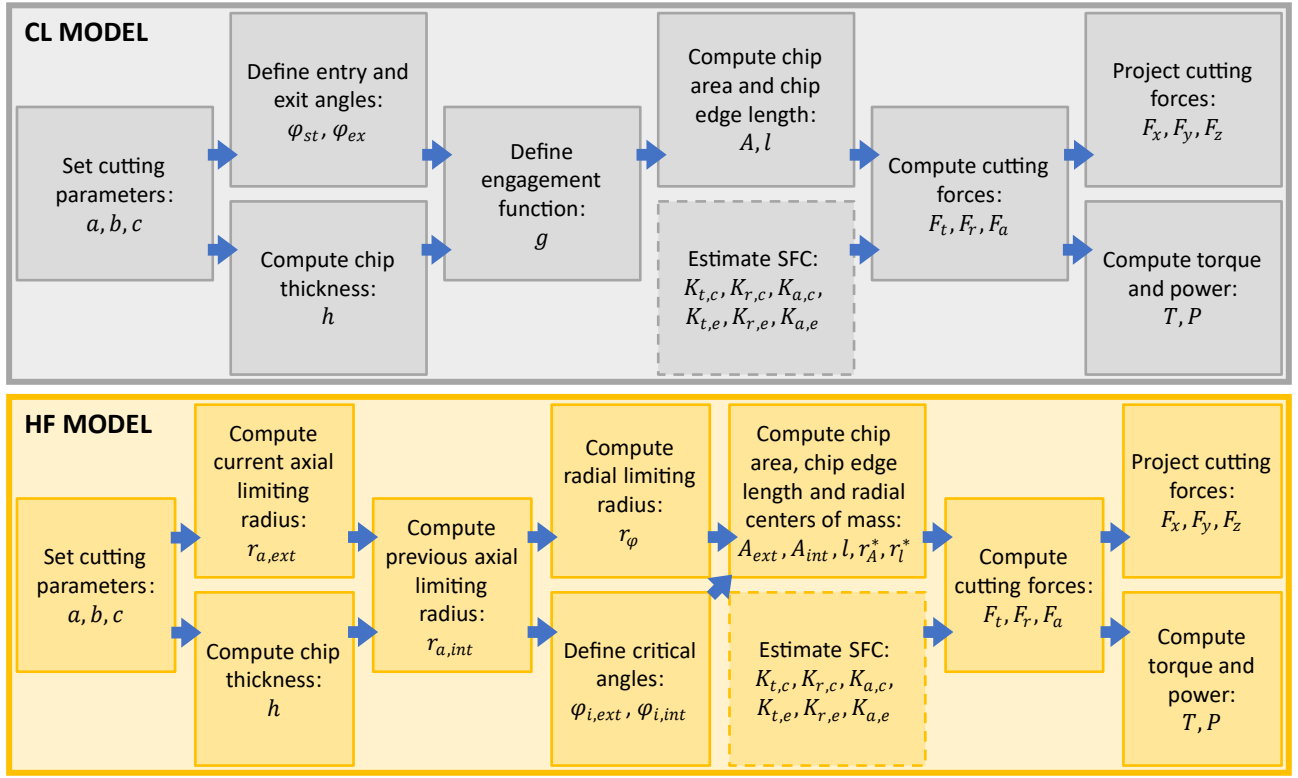


Figure 4: Flow chart representing the needed steps to compute instantaneous cutting quantities (forces, torque and power) for the CL (appendix A) and HF (section 2.1) models. Estimation of the SFC (dashed boxes) must be performed beforehand.

A_{ext} , l , $r_{A,j}^*$ and $r_{l,j}^*$ were reported in appendix B, while a_{do} terms in C, due to their complexity. The different implementation of the CL and HF models was summarized in figure 4. The figure represents the step-by-step computations to be performed in order to calculate instantaneous cutting forces, torque and power.

2.2. Experimental set-up and Design of Experiments

The experimental set-up available was shown in figure 5. A Mandelli M5 machining centre was used, equipped with a Mitsubishi AJX06R203SA20S high-feed mill, with three JOMT06T216ZZER-JL MP9140 cutting inserts. The adopted cutters presented a nominal diameter equal to 20 mm. Their geometry featured two consecutive phases with lead angles equal to 12.5° and 24.5°. The cutter parameters after the geometrical simplification introduced by the model discussed in section 2.1 were reported in table 1. A Kistler

Table 1

Cutter geometrical parameters.

r_1 [mm]	r_2 [mm]	r_3 [mm]	r_4 [mm]	z_1 [mm]	z_2 [mm]	z_3 [mm]	z_4 [mm]
5.35	6.57	8.53	9.03	0	0	0.40	0.62

9255B dynamometric plate was adopted for the milling forces measurement, followed by a Kistler 5070 charge amplifier. A three-phase power meter was used to acquire the spindle

power (with three LEM LF 205-S/SP3). These quantities were acquired through a NI cRIO 9039, with a NI 9215 acquisition card for cutting forces and NI 9205 acquisition card for spindle power. Siemens SinuCom NC was used to acquire the spindle quadrature current and speed, axis positions and speeds. Cutting forces were acquired at high frequency (5 kHz), while SinuCom quantities were acquired at 250 Hz.

In order to experimentally identify the SFC from the two analytical models (i.e. CL and HF), a set of 48 experiments was designed, constituted by 4 replicates of 12 different cutting conditions (table 2, fig. 1G). Tests were performed on a Ti_6Al_4V rectangular workpiece of dimensions 255x262 mm. DoE consisted of two a levels: 0.4 and 0.6 mm. The a levels were chosen so that the first one was keeping only the first phase of the cutting edge engaged, while the highest level included also the cutting edge second phase. Five levels of c were adopted: 0.60, 0.65, 0.70, 0.75 and 0.80 mm/tooth. Three levels of cutting speed v_c were chosen 50, 60 and 70 m/min. All the tests were performed at $b = 13$ mm. The number of experiments was chosen in order to allow for a good estimation of SFC, following [63, 64, 65, 66, 67]. Five levels of c were chosen to explore the range of applicability of the tool, suggested by the tool manufacturer, and catch the trend of mean forces [63]. Cutting speed was varied in order to take into account the process variability. The parameter combinations were shown in table 2.

The cuts with ID 4 and 10 were chosen as validation data.

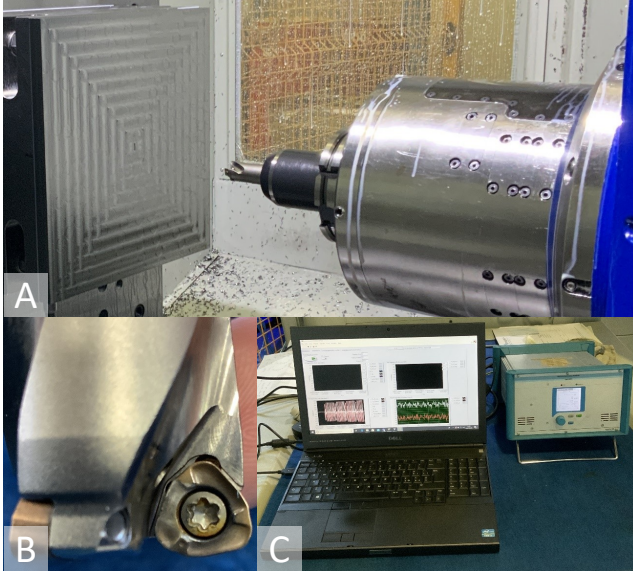


Figure 5: Experimental set-up: A) Ti_6Al_4V workpiece and mill; B) Mitsubishi high-feed mill; C) DAQ.

Table 2

Design of Experiments parameter combinations.

ID	c [mm/tooth]	a [mm]	v_c [m/min]	n [rpm]	Replicates	Model use
1	0.75	0.40	50	796	4	fitting
2	0.80	0.40	50	796	4	fitting
3	0.60	0.40	50	796	4	fitting
4	0.65	0.40	55	955	4	validation
5	0.70	0.40	70	1114	4	fitting
6	0.70	0.40	50	796	4	fitting
7	0.75	0.60	50	796	4	fitting
8	0.80	0.60	50	796	4	fitting
9	0.60	0.60	50	796	4	fitting
10	0.65	0.60	55	955	4	validation
11	0.70	0.60	70	1114	4	fitting
12	0.70	0.60	50	796	4	fitting

This was in accordance with reference literature in similar applications (e.g. SFC identification [62]) and linear regression problems [68]. Validation tests featured parameters that were unseen in model fitting experiments in terms of c and v_c . This choice was taken in order to verify linearity hypothesis and checking prediction accuracy. The regressor values for validation were determined in order to use the linear regression model for interpolation, and not for extrapolation (being this a general rule of applicability for linear regression models). In fact, by using the model for extrapolation, the assumptions can't be verified and the prediction intervals (PI) naturally increase [69]. The axial depth of cut a was considered as a block factor, while all the tests were casualized within each block.

2.2.1. Model Identification

Model identification procedure was firstly proposed by Altintas [21]. It consists in a multivariate linear regression

problem (from which the notation is adopted [69]). This allows estimating the SFC (fig. 1E-F). The fitting procedure exploits the mean cutting forces measured during the experiments. The systems of linear equations A.5 and 13 can be written in matrix fashion (eq. 16):

$$\begin{Bmatrix} \bar{F}_x \\ \bar{F}_y \\ \bar{F}_z \end{Bmatrix} = \begin{bmatrix} x_{11} & x_{12} & \dots & x_{16} \\ x_{21} & x_{22} & \dots & x_{26} \\ x_{31} & x_{32} & \dots & x_{36} \end{bmatrix} \cdot \begin{Bmatrix} K_{t,c} \\ K_{t,e} \\ K_{r,c} \\ K_{r,e} \\ K_{a,c} \\ K_{a,e} \end{Bmatrix} \quad (16)$$

If M tests are experimented, the identification problem can be rewritten in a multivariate linear regression fashion (eq. 17):

$$\begin{Bmatrix} \bar{F}_{x,1} \\ \bar{F}_{y,1} \\ \bar{F}_{z,1} \\ \bar{F}_{x,2} \\ \bar{F}_{y,2} \\ \bar{F}_{z,2} \\ \dots \\ \bar{F}_{x,M} \\ \bar{F}_{y,M} \\ \bar{F}_{z,M} \end{Bmatrix} = \begin{bmatrix} x_{11,1} & x_{12,1} & \dots & x_{16,1} \\ x_{21,1} & x_{22,1} & \dots & x_{26,1} \\ x_{31,1} & x_{32,1} & \dots & x_{36,1} \\ x_{11,2} & x_{12,2} & \dots & x_{16,2} \\ x_{21,2} & x_{22,2} & \dots & x_{26,2} \\ x_{31,2} & x_{32,2} & \dots & x_{36,2} \\ \dots & \dots & \dots & \dots \\ x_{11,M} & x_{12,M} & \dots & x_{16,M} \\ x_{21,M} & x_{22,M} & \dots & x_{26,M} \\ x_{31,M} & x_{32,M} & \dots & x_{36,M} \end{bmatrix} \cdot \begin{Bmatrix} K_{t,c} \\ K_{t,e} \\ K_{r,c} \\ K_{r,e} \\ K_{a,c} \\ K_{a,e} \end{Bmatrix} + \begin{Bmatrix} \epsilon_1 \\ \epsilon_2 \\ \dots \\ \epsilon_M \end{Bmatrix} \quad (17)$$

$$\mathbf{y} = \mathbf{X}_k \boldsymbol{\beta}_k + \boldsymbol{\epsilon}_k$$

where $k = CL, HF$; \mathbf{y} is the vector of responses, i.e. mean forces; \mathbf{X}_k is the design matrix of either CL and HF model; $\boldsymbol{\beta}_k$ is the vector of regression coefficients, i.e. SFC; $\boldsymbol{\epsilon}_k$ is the vector of residuals with $\epsilon_{m,k} \sim \mathcal{N}(0, \sigma_k^2)$ uncorrelated random variables. The Ordinary Least Squares estimates for SFC are given by equation 18:

$$\hat{\boldsymbol{\beta}}_k = (\mathbf{X}_k^T \mathbf{X}_k)^{-1} \mathbf{X}_k^T \mathbf{y}, \quad k = CL, HF \quad (18)$$

The reconstructed responses are (eq. 19):

$$\hat{\mathbf{y}}_k = \mathbf{X}_k \hat{\boldsymbol{\beta}}_k, \quad k = CL, HF \quad (19)$$

The estimated residuals are (eq. 20):

$$\mathbf{e}_k = \mathbf{y} - \hat{\mathbf{y}}_k, \quad k = CL, HF \quad (20)$$

It is then possible to estimate the variance of the process errors as (eq. 21):

$$\hat{\sigma}_k^2 = \frac{\mathbf{e}_k^T \mathbf{e}_k}{n_p - p}, \quad k = CL, HF \quad (21)$$

where n_p is the number of data points (i.e. $3M$) and p the number of regression coefficients (i.e. 6 SFC). It is possible also to compute the covariance matrix of the regression coefficients $\boldsymbol{\Sigma}_{\boldsymbol{\beta}_k}$ (eq. 22):

$$\boldsymbol{\Sigma}_{\boldsymbol{\beta}_k} = \hat{\sigma}_k^2 \mathbf{C}_k, \quad k = CL, HF \quad (22)$$

where \mathbf{C}_k is the matrix $(\mathbf{X}_k^T \mathbf{X}_k)^{-1}$. Process variance allows for the computations of the regression coefficients 100 $(1 - \alpha)\%$ confidence intervals (CI) through equation 23 (fig. 1H):

$$\hat{\beta}_{k,o} - t_{\alpha/2, n_p-p} \sqrt{\hat{\sigma}_k^2 C_{oo,k}} \leq \beta_{k,o} \leq \hat{\beta}_{k,o} + t_{\alpha/2, n_p-p} \sqrt{\hat{\sigma}_k^2 C_{oo,k}} \quad (23)$$

where $k = CL, HF$; α is the significance level, $C_{oo,k}$ is the o -th element of the diagonal of matrix \mathbf{C}_k ; $t_{\alpha/2, n_p-p}$ is the upper $\alpha/2$ percentage point of a t distribution with $n_p - p$ degrees of freedom. Such limits are then the CI extrema for SFC.

2.3. Model Validation

Four main procedures were followed for the assessment and validation of the developed HF model (fig. 1I-J-K-L).

2.3.1. First validation step

This procedure consisted in the prediction of mean forces on model fitting and validation data (fig. 1I). 100 $\cdot (1 - \alpha)\%$ PI for single new response observations were computed through equation 24 [69]:

$$\begin{aligned} \hat{y}(\mathbf{x}_{0,k}) - t_{\alpha/2, n_p-p} \sqrt{\hat{\sigma}_k^2 \left(1 + \mathbf{x}_{0,k}^T \mathbf{C}_k \mathbf{x}_{0,k}\right)} \\ \leq y_0 \leq \hat{y}(\mathbf{x}_{0,k}) + t_{\alpha/2, n_p-p} \sqrt{\hat{\sigma}_k^2 \left(1 + \mathbf{x}_{0,k}^T \mathbf{C}_k \mathbf{x}_{0,k}\right)} \end{aligned} \quad (24)$$

where $\mathbf{x}_{0,k}$ is the new point for which an estimated response is required, with $k = CL, HF$; $\hat{y}(\mathbf{x}_{0,k})$ is the estimated response $\mathbf{x}_{0,k}^T \hat{\beta}_k$.

2.3.2. Second validation step

This validation procedure consisted in the multivariate hypothesis testing of SFC estimates (fig. 1J). Since the CL and HF models are based on SFC carrying the same physical meaning, a statistical hypothesis testing procedure was applied to test whether or not the two models shown any statistically appreciable difference. In this case, two steps were applied: first of all, the Box M test for covariance equality [70] was applied to the two SFC groups. Since Box M test rejected the covariance equality in null hypothesis at 0.05 significance, an alternative to the Hotelling's Two-Sample T-squared test for difference in means was used. Nel and van der Merwe [71] procedures to solve Behrens-Fisher multivariate tests were adopted at 0.05 significance. Simultaneous CI for each difference between CL and HF SFC were computed at 0.05, highlighting the directions of meaningful differences.

2.3.3. Third and fourth validation steps

These steps were reported in the same section due to their similar methodology. The difference between the two, is that they are based on the prediction of two different physical quantities: the mean spindle cutting torque (fig. 1K) and the

mean spindle cutting power (fig. 1L). Such quantities were used for validation since none of them was introduced in the model fitting procedure. In this way, a more robust validation approach was introduced. The new variables were expressed as functions of the SFC, in order to make predictions. Starting from the CL model, mean torque and mean power follow equation 25 and 26:

$$\begin{aligned} \hat{T}_{CL} &= r_{nom} \{x_{35,CL} \ x_{36,CL} \ 0 \ 0 \ 0 \ 0\} \hat{\beta}_{CL} = \\ &= \mathbf{a}_{T,CL}^T \hat{\beta}_{CL} \end{aligned} \quad (25)$$

$$\begin{aligned} \hat{P}_{CL} &= 2\pi n r_{nom} \{x_{35,CL} \ x_{36,CL} \ 0 \ 0 \ 0 \ 0\} \hat{\beta}_{CL} = \\ &= \mathbf{a}_{P,CL}^T \hat{\beta}_{CL} \end{aligned} \quad (26)$$

where $x_{do,CL}$ is the predictor in row d and column o of the matrix in equation 16 for the CL model, computed at the nominal cutting parameters of a given experiment; $\mathbf{a}_{T,CL}^T$ is defined as $\{x_{35,CL} \ x_{36,CL} \ 0 \ 0 \ 0 \ 0\}$ and $\mathbf{a}_{P,CL}^T$ is defined as $2\pi n r_{nom} \{x_{35,CL} \ x_{36,CL} \ 0 \ 0 \ 0 \ 0\}$.

For the HF model, it is necessary to take the mean over a tool revolution of the instantaneous torque (eq. 15) and power (substituting equation 15 in equation A.7):

$$\hat{T}_{HF} = \frac{1}{T_P} \int_0^{T_P} T(t) dt = \mathbf{a}_{T,HF}^T \hat{\beta}_{HF} \quad (27)$$

$$\hat{P}_{HF} = \frac{1}{T_P} \int_0^{T_P} P(t) dt = \mathbf{a}_{P,HF}^T \hat{\beta}_{HF} \quad (28)$$

where the integrals can be expressed as two vectors $\mathbf{a}_{T,HF}^T$ and $\mathbf{a}_{P,HF}^T$ multiplied by the estimated SFC. It is then possible to propagate the uncertainty of the SFC estimations to the new variables of interest (eq. 25-28). Being the mean torque and mean power linear combinations of the SFC, the uncertainty is propagated through equation 29 [72]:

$$s_{q,k}^2 = \mathbf{a}_{q,k}^T \mathbf{\Sigma}_{\beta_k} \mathbf{a}_{q,k} \quad (29)$$

where q stands for the quantity of interest, i.e. either T or P ; k stands for the reference model, i.e. CL or HF; $s_{q,k}^2$ is the variance associated to the quantity q prediction using the k -th model; $\mathbf{a}_{q,k}$ is the vector that transforms SFC in the variable of interest (eq. 25-28); $\mathbf{\Sigma}_{\beta_k}$ is the covariance matrix of the SFC coefficients (22).

3. Results and discussion

In this section, the results of the analysis of the experimental campaign data will be reported and discussed. The presentation of the results will start with the instantaneous forces prediction capabilities, followed by the three validation steps described in section 2.

Table 3

Identification of SFC for CL and HF models, together with their associated 95% CI.

SFC	CL			HF		
	Lower	Mean	Upper	Lower	Mean	Upper
$K_{t,c}$ [MPa]	969.7	1696.5	2423.3	1084.5	1255.2	1426.0
$K_{t,e}$ [N/mm]	-114.8	262.1	639.1	70.0	86.5	103.1
$K_{r,c}$ [MPa]	-523.5	203.3	930.0	135.5	306.3	477.0
$K_{r,e}$ [N/mm]	-181.8	195.1	572.0	-0.9	15.7	32.2
$K_{a,c}$ [MPa]	190.2	845.8	1501.4	-194.1	-39.2	115.8
$K_{a,e}$ [N/mm]	422.8	746.9	1070.9	191.7	205.9	220.2

Table 4

ANOVA tables comparisons for CL and HF regression models.

Source	DF	Seq SS	Contribution	Adj SS	Adj MS	F-Value	P-Value
Regression	6	20203366	98.92%	20203366	3367228	1743.79	0.000
Ktc	1	8566401	41.94%	41291	41291	21.38	0.000
Kte	1	265945	1.30%	3665	3665	1.90	0.171
Krc	1	74264	0.36%	593	593	0.31	0.581
Kre	1	2030	0.01%	2030	2030	1.05	0.307
Kac	1	11254475	55.11%	12612	12612	6.53	0.012
Kae	1	40252	0.20%	40252	40252	20.85	0.000
Error	114	220132	1.08%	220132	1931		
Lack-of-Fit	18	201960	0.99%	201960	11220	59.27	0.000
Pure Error	96	18172	0.09%	18172	189		
Total	120	20423498	100.00%				

(a) CL model.

Source	DF	Seq SS	Contribution	Adj SS	Adj MS	F-Value	P-Value
Regression	6	20396977	99.87%	20396977	3399496	14612.50	0.000
Ktc	1	8738358	42.79%	49331	49331	212.05	0.000
Kte	1	60524	0.30%	24944	24944	107.22	0.000
Krc	1	132467	0.65%	2936	2936	12.62	0.001
Kre	1	821	0.00%	821	821	3.53	0.063
Kac	1	11274175	55.20%	58	58	0.25	0.617
Kae	1	190632	0.93%	190632	190632	819.42	0.000
Error	114	26521	0.13%	26521	233		
Lack-of-Fit	18	8349	0.04%	8349	464	2.45	0.003
Pure Error	96	18172	0.09%	18172	189		
Total	120	20423498	100.00%				

(b) HF model.

3.1. Model identification

The model fitting procedure allowed to identify the SFC values and the associated 95% CI, which are reported in table 3. The fitting procedures computational times resulted to be 12.3 ms and 46.7 ms for the CL and HF models, respectively. The computational times included the design matrix construction and the SFC identification. In order to provide a reliable estimate, they were reported as the average over 10000 cycles. Furthermore, such cycles were performed using Matlab® on a Dell XPS 15 7590 featuring an Intel® Core™ i7-9750H CPU @ 2.60GHz.

It is clear how the developed HF model is capable of better catching the physical phenomenon underneath the cut than the CL one. In fact, identified SFC with HF model

present narrower 95% CI. This means that the uncertainty in the estimation of the SFC is lower and it is confirmed even by the significance tests for the single regressors. Such tests can be checked directly from the CI of each regressor: a regressor results to be significant on the associated hypothesis test at 0.05 significance level (i.e. the regression coefficient is significantly different from 0), if its 95% CI doesn't include 0. Analysis of Variance (ANOVA) tables for the CL (table 4a) and HF (table 4b) regression models were computed through Minitab software.

The p-values of the single regression coefficient significance were explicitly shown in such tables. Using CL model, three SFC were not significant at 0.05 significance level (i.e. $K_{t,e}$, $K_{r,c}$ and $K_{r,e}$), whereas only two using the HF model

Table 5
Model performance summaries comparison.

Model	S	R-sq	R-sq(adj)	PRESS	R-sq(pred)	AICc	BIC	Test S	Test R-sq
CL	43.9429	98.92%	98.87%	240795	98.82%	1257.28	1275.80	41.1673	98.89%
HF	15.2526	99.87%	99.86%	29221	99.86%	1003.33	1021.84	15.2180	99.85%

(i.e. $K_{r,e}$ and $K_{a,c}$). It is possible also to note the amount of variance explained by the two regression models, i.e. R-squared (on model fitting data), looking at the *regression* row in *contribution* field. For both the models, R-squared is really high and comparable: 98.92% for the CL model versus 99.87% for the HF model. Usually, even adjusted R-squared, prediction R-squared and Test R-squared are computed, since they provide a more reliable information on the performances of the regression models. Adjusted R-square takes into account also the number of used predictors (in this case both the models use six regressors, so adjusted R-squared and R-squared provide the same information in the comparison of the two models). Prediction R-squared is computed by leaving out one sample per time from the fitting procedure, and tells how good a model is in explaining the variance for new predictions. Such coefficient is related to a leave-one-out cross-validation procedure for evaluating the model prediction capabilities and makes use of the PRESS statistic [73, 74]. Test R-squared has the same meaning of R-squared but it is computed only on model validation data, so it tells how much variability is explained by the model on a completely new set of data. The comparison between these coefficients for both the models is reported in table 5.

Figures 6a and 6b represent instead the diagnostics of the regression analysis performed with CL and HF models, respectively. The top-left graph (A) is the quantile-quantile graph for normal distributions. It is used to check qualitatively the normality assumption of residuals together with the bottom-left graph (C), which represents the discrete probability density function of residuals. If data follow a normal distribution, they fall close to the red straight line. These graphs are typically accompanied by normality hypothesis tests. Here, Anderson-Darling (AD) normality test was performed on model fitting residuals. The results of the tests were reported in table 6. AD test assumes under the null hypothesis that the data follow a normal distribution. The p-value for CL residuals is 0.012 meaning that at 0.05 significance level, the null hypothesis is rejected. AD didn't reject the null hypothesis for the developed HF model, having a p-value of 0.199. This is another proof that the HF model is better representing the mean force data. The top-right graph (B) shows the residuals of regression versus the fitted values of mean forces. The interpretation of such graph is similar to the one in the bottom right corner (D), representing the residuals versus the experiment number. Looking at figure 6, it seems that homoscedasticity (i.e. model fitting residuals constant variance) is verified for both the models. Independence of model fitting residuals is not verified for the

Table 6
Anderson-Darling normality tests.

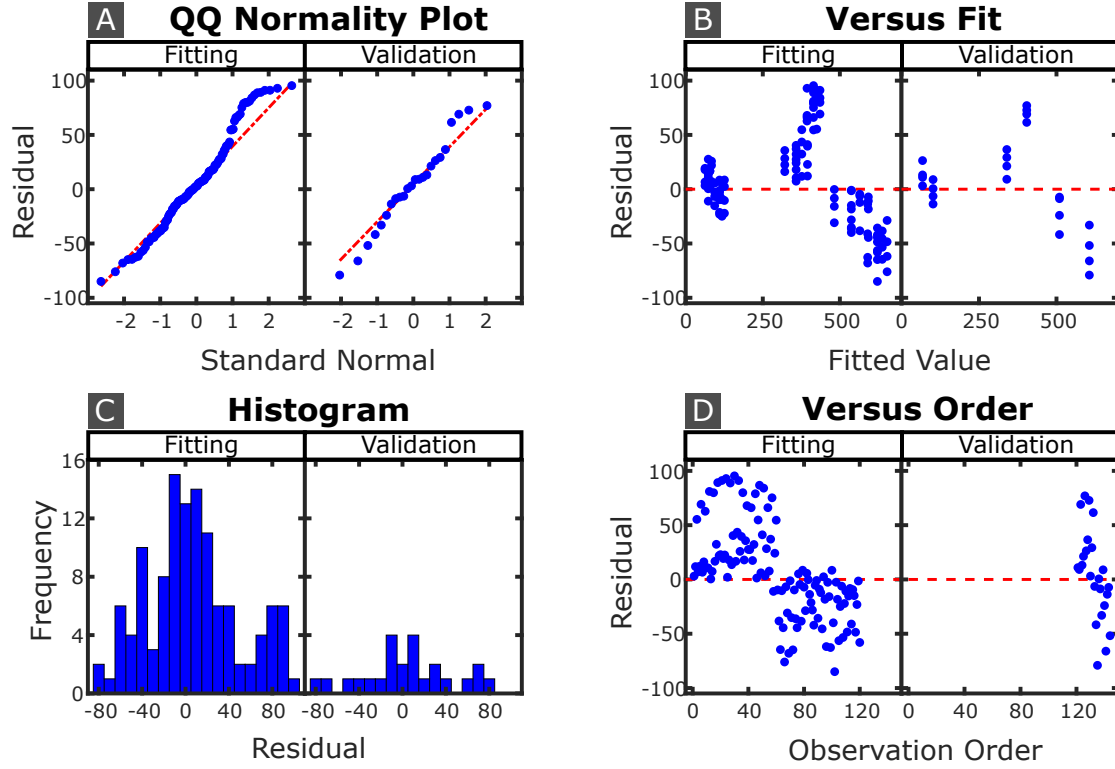
Model	Mean	StDev	N	AD	p-value
CL	6.470	42.52	120	0.995	0.012
HF	0.279	14.93	120	0.505	0.199

CL model, where residuals from observation number 1 to 60 are over the 0 line, while residuals from 61 to 120 are below the 0 line.

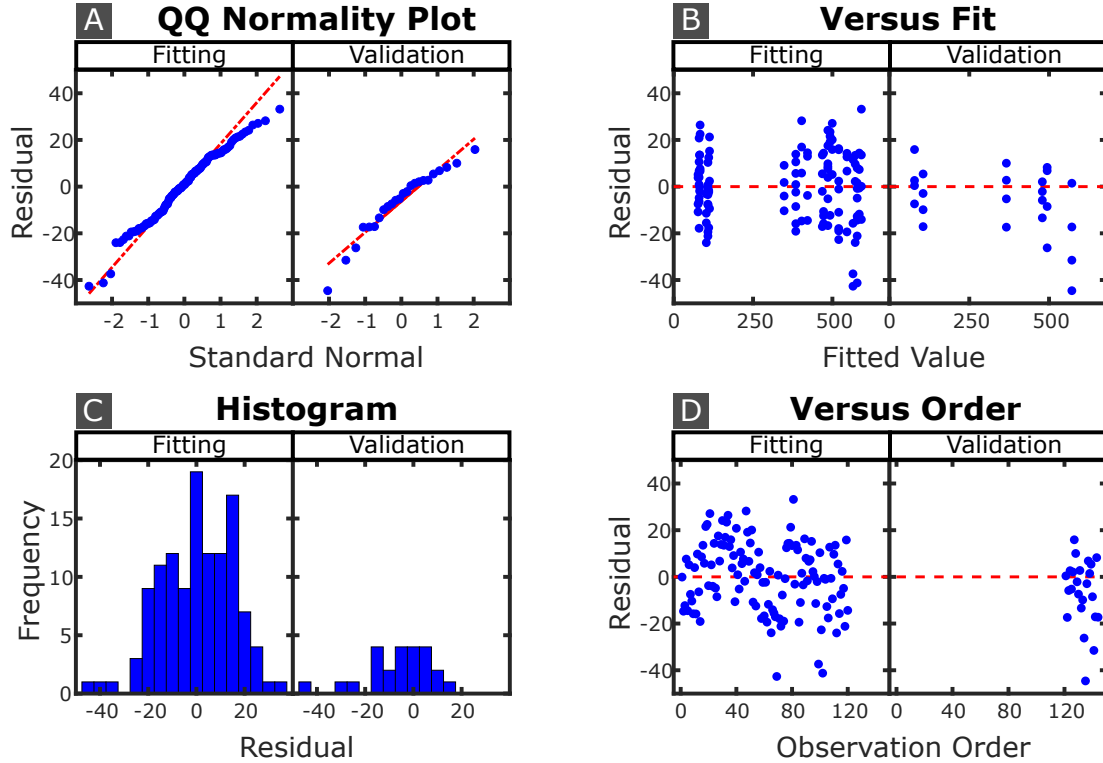
The different behaviour of the two models is also evident in the predicted instantaneous cutting forces. Figures 7a and 7b highlight the improved accuracy of the developed model in the description of the variable entry angles of the cutting inserts. In fact, the CL model features a portion of about 12° where no cutting inserts were engaged. On the contrary, the HF model correctly identifies a continuous cutting condition, where a cutting insert starts engaging the workpiece right in the moment where the previous one is exiting from it. This came from a peculiar choice in the nominal engagement b , determined to have exactly one cutter per time engaged in the workpiece. Nevertheless, it must be noted that the model catches a nominal behaviour of the instantaneous cutting forces, while experimental forces didn't show a null instantaneous force sample. This should be attributed to the dynamical components of the cutting process and to the run-out of the cutting tool. Radial vibrations of the tool tip cause small deviations in the radial engagement of the mill, causing a small delay between the entry of a cutter and the exit of the previous one. Radial cutters run-out causes small changes in their entry and exit angles, providing a similar effect. Furthermore, two other main considerations have to be brought to the reader attention: (i) the conceived model is, in general, better predicting the magnitude of the cutting forces; (ii) the HF model predictions for instantaneous cutting forces are featured by narrower 95% PI, due to the higher confidence in the regression coefficients estimation.

3.2. Model validation first step

The behaviour pointed out in the last section is associated to the change in the axial depth of cut. For $a = 0.4 \text{ mm}$ the model is underestimating the mean cutting forces, while for $a = 0.6 \text{ mm}$ the model is overestimating them. The HF model is instead capable of well representing the mill cutting operation under both the axial depths of cut. This behaviour of the two models can be easily identified by looking at the mean force regression surfaces in the plane $a-c$. Such

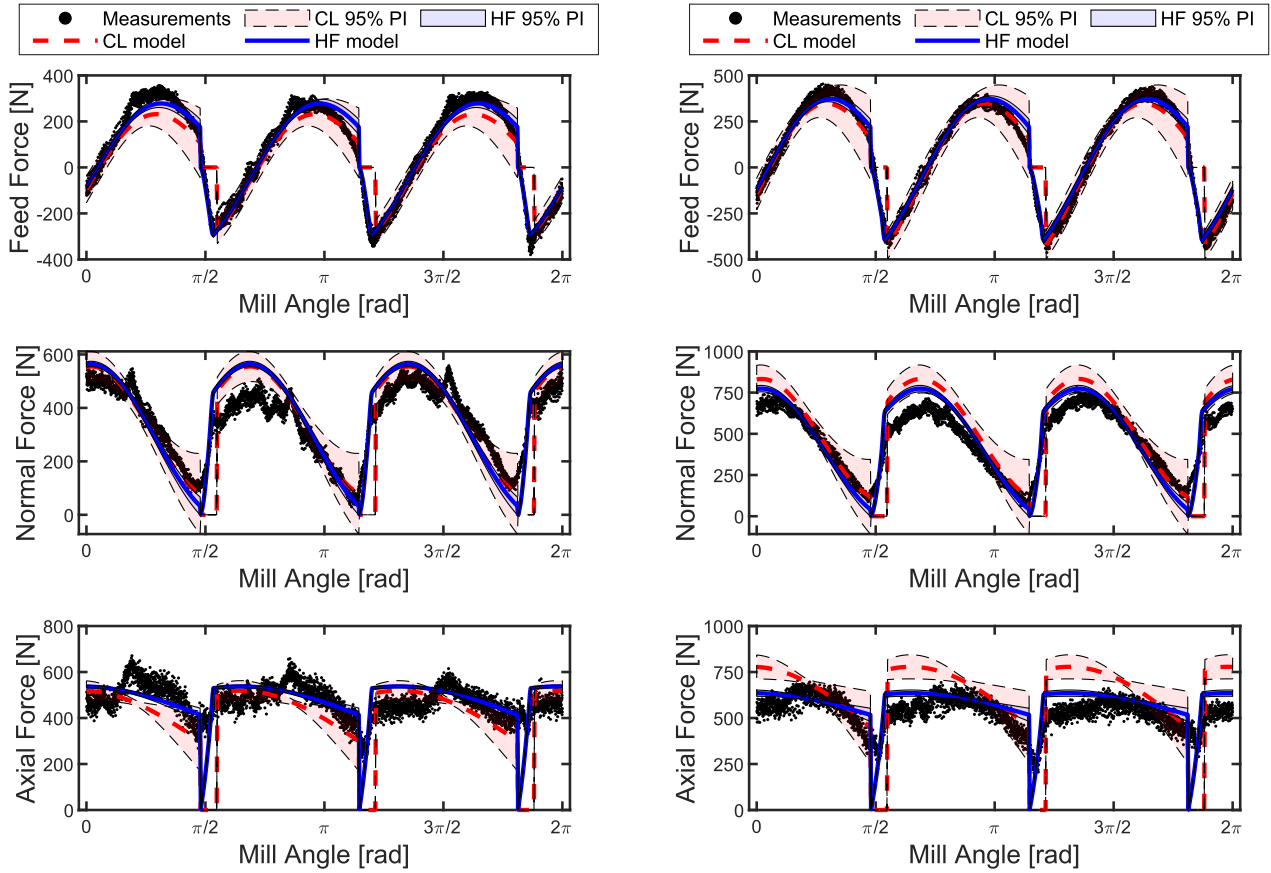


(a) CL model.



(b) HF model.

Figure 6: Diagnostics of regression analysis. Quantiles-quantiles normality plot (A): the more residuals follow a normal distribution, the more the blue points lay on the red line. Residuals versus fitted responses (B): blue points should be randomly distributed around the red line to indicate their independence. Residuals histograms (C): should be as close as possible to a gaussian probability density function. Residuals versus observation (D): they should be randomly distributed and show constant variance.



(a) Test ID 4: $a = 0.4 \text{ mm}$, $c = 0.65 \text{ mm/tooth}$ and $v_c = 55 \text{ m/min}$. (b) Test ID 10: $a = 0.6 \text{ mm}$, $c = 0.65 \text{ mm/tooth}$ and $v_c = 55 \text{ m/min}$.

Figure 7: Instantaneous force predictions of CL (dashed red line) and HF (solid blue line) models with respect to the mill angle. Coloured bands represent prediction intervals of the forces components and are drawn with analogous line style and colour.

graphs are reported in figures 8a-8b, for the CL and HF models, respectively.

In fact, the developed HF model includes two different behaviours, related to a lower then z_3 and a bigger than z_3 (i.e. the beginning of the engagement of the cutting edge second phase). Such distinction is visible in the response surface of the HF model (8b, red arrow). In correspondence of $a = z_3 = 0.4 \text{ mm}$, the response surface is featured by a sudden transition, due to the second cutting edge phase and to the modified chip geometry included in the model. The same wasn't observed in the CL model. This novelty allows the HF model to catch the different behaviours of the HF mills at different a values and not to under/overestimate the mean forces in the tested conditions. This phenomenon is even clearer while looking at the response curves of the two models at the tested a values, in a two-dimensional plot (figures 9a-9d). From these figures, it is evident the difference between the two models. To quantitatively compare the two models, the Root Mean Squared Prediction Error (RMSPE - root mean squared error on the prediction of model validation data) was computed [75, 76]. The proposed model resulted to be remarkably more precise than the CL model, with an RMSPE of 15 N against 41 N , respectively. The as-

sociated model validation maximum errors (in module) were 44 N for HF and 79 N for CL. Narrower SFC confidence intervals presented in table 3 translate in more accurate PI for the mean forces. Then, HF model is able to more reliably predict the mean cutting forces than the CL model. These results were confirmed also by the Mean Absolute Percentage Error (MAPE) metric [77, 78]. In fact, the MAPE obtained with the CL model was 9.9%, whereas the HF model allowed to reach a smaller value of 4.6%. Thus, the HF model dramatically decreased the MAPE on the validation tests, providing reliable predictions of mean forces.

3.3. Model validation second step

In order to statistically evaluate the difference between the two models, multivariate hypothesis testing was applied to the estimated regression coefficients. Literature proposes two approaches in order to compare the regression coefficients of two models [79]. The first one consists in the application of univariate 2t-tests on each pair of regression coefficients mean [80]. The second approach uses a joint ANOVA on the data, adding a categorical variable that assigns the data to the correspondent model. Interaction terms must be included in such regression problem [81]. The first approach

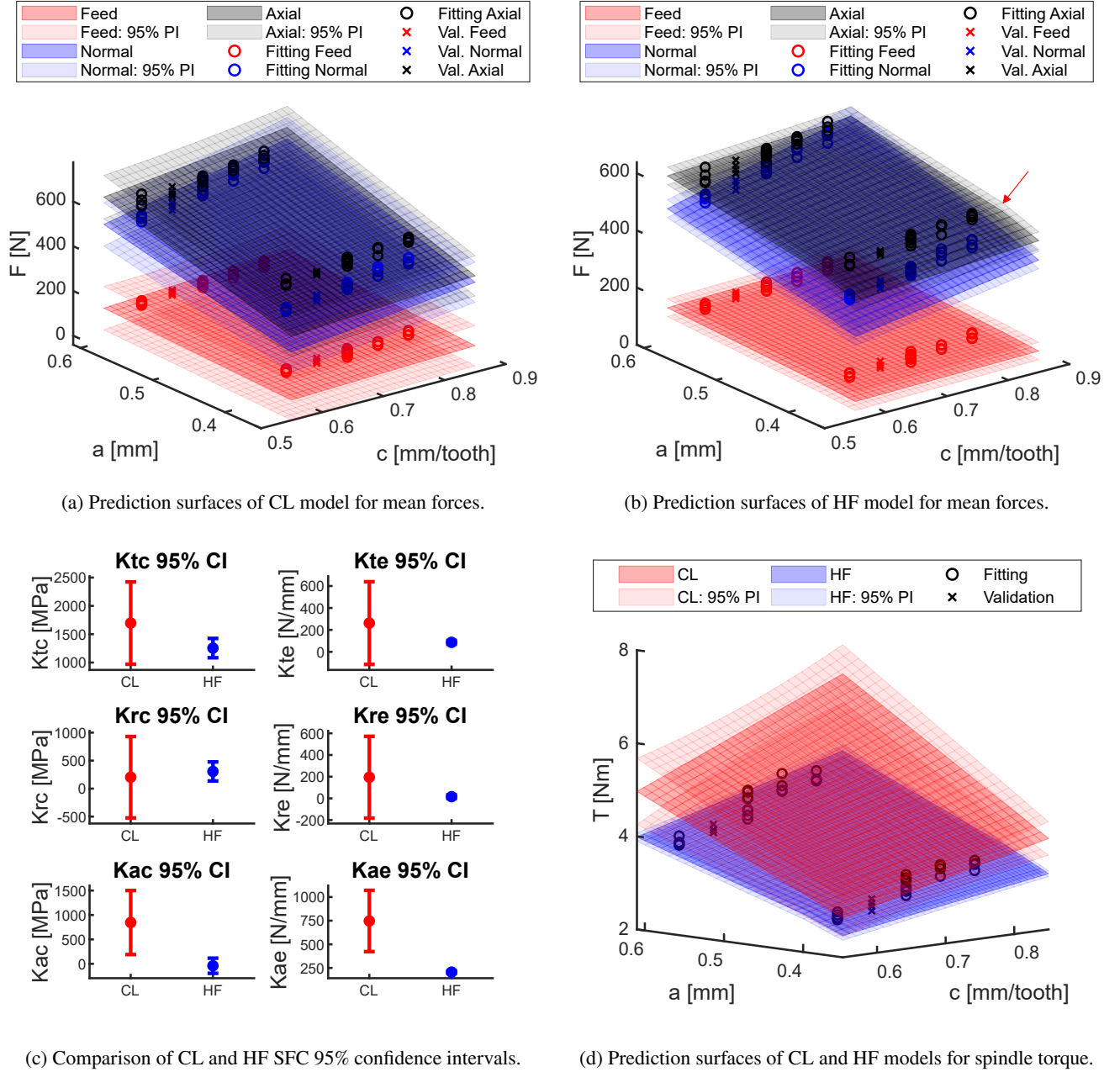


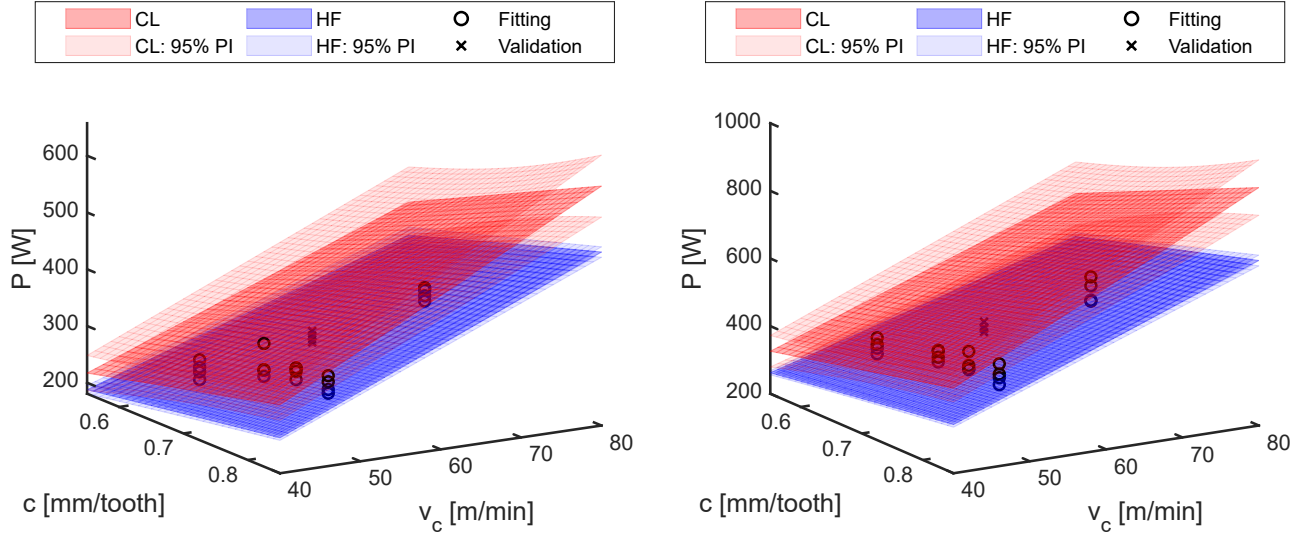
Figure 8: Comparison summary between the CL and HF model for all the validation steps. (a) and (b) represent the first validation step, comparing the prediction capability of the two models with respect to mean forces. (c) summarizes the second validation step, comparing the confidence intervals for the SFC estimation. (d) compares the prediction capabilities with respect to the mean torque, while (e) and (f) with respect to the mean power (thus, constituting the summary of the third validation step).

is less conservative and tends to refuse the null hypothesis more frequently. This comes from the fact that the SFC are treated in a univariate fashion, while they are actually part of the same covariate set. Here, an extension of the method was proposed applying a multivariate approach. Box M test results were reported in table 7. The test refused the null hypothesis and, then, covariance equality of the CL and HF SFC. Because of such result, it was not possible to apply the classical Hotelling's T-squared test. The comparison be-

Table 7

Box M test for covariances equality.

DF1	DF2	F	p-value
21	187857	142.00	0.000



(e) Prediction surfaces of CL and HF models for spindle power ($a = 0.4$ mm).

(f) Prediction surfaces of CL and HF models for spindle power ($a = 0.6$ mm).

Figure 8: Comparison summary between the CL and HF model for all the validation steps. (a) and (b) represent the first validation step, comparing the prediction capability of the two models with respect to mean forces. (c) summarizes the second validation step, comparing the confidence intervals for the SFC estimation. (d) compares the prediction capabilities with respect to the mean torque, while (e) and (f) with respect to the mean power (thus, constituting the summary of the third validation step). (cont.)

Table 8

Nel and van der Merwe procedures for Behrens-Fisher multivariate test for mean equality.

DF1	DF2	F	p-value
6	169	17090.49	0.000

tween the means of the SFC was carried out through Nel and van der Merwe procedures to Behrens-Fisher multivariate tests [71]. The results of the test were reported in table 8. The p-value of the test was null, underlying statistical evidence about the difference in the HF and CL SFC means. It was then possible to compute the 95% simultaneous confidence intervals for the differences between each SFC pair. The intervals were reported in table 9. The intervals for the difference in means didn't include the zero, except for $K_{r,c}$. Then, the means of the SFC between CL and HF models were statistically different except for $K_{r,c}$. Such results confirmed that the CL model was not able to catch the physical phenomenon underneath high-feed milling and further supported the need for the developed HF model. The difference between the estimated SFC using CL and HF models was highlighted by figure 8c. It is clear also from this figure that $K_{r,c}$ was the only equal SFC. The identified HF $K_{t,c}$ resulted to be significantly lower than the CL one. This difference is probably due to the fact that the HF model takes into account a much longer edge contact length, reflecting in

Table 9

95% confidence intervals for mean differences between CL and HF SFC.

SFC Difference	Lower	Upper
$\Delta K_{t,c}$ [MPa]	-566.5	-316.0
$\Delta K_{t,e}$ [N/mm]	-238.9	-112.3
$\Delta K_{r,c}$ [MPa]	-22.3	228.2
$\Delta K_{r,e}$ [N/mm]	-242.7	-116.1
$\Delta K_{a,c}$ [MPa]	-998.0	-772.0
$\Delta K_{a,e}$ [N/mm]	-595.4	-486.5

a wider contribution of the ploughing effect under the flank face of the cutting edge. Of course, being the edge contact length longer, even the $K_{t,e}$ assumes a lower value. The axial force is dominated by the ploughing effects. The opposite occurs for the radial components which are basically constituted by the shearing action on the shearing plane.

3.4. Model validation third and fourth steps

To further validate the model, the prediction of variables of technological interest not included in the fitting procedure was carried out. Spindle torque and power are in fact useful to assess the feasibility of an operation on the available machine tool. The prediction surfaces of the spindle torque for the CL and HF model were reported in figure 8d.

It is evident that the HF model outperformed the CL one both in the mean torque prediction as well as in the confi-

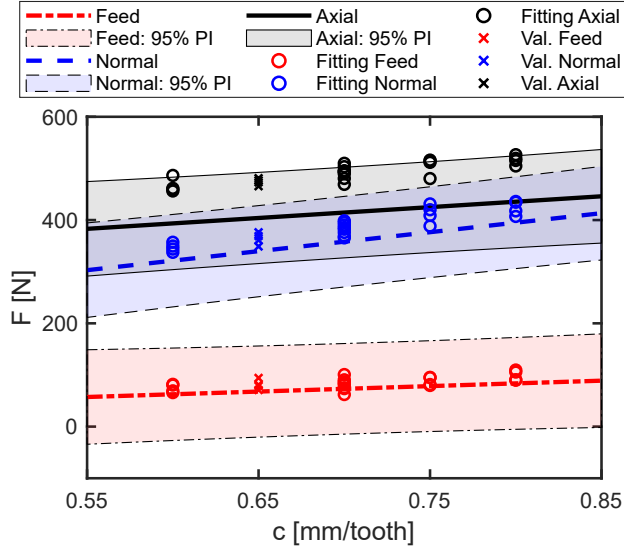
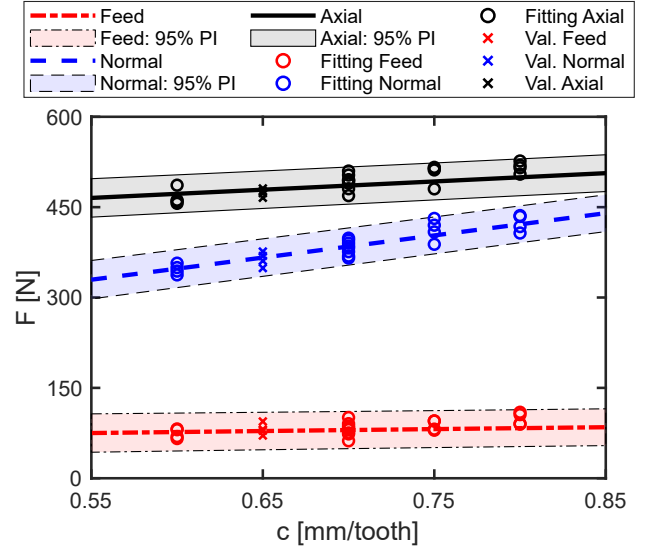
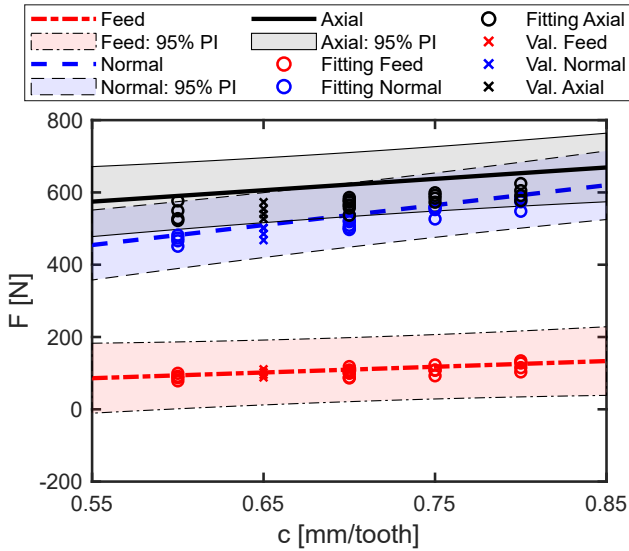
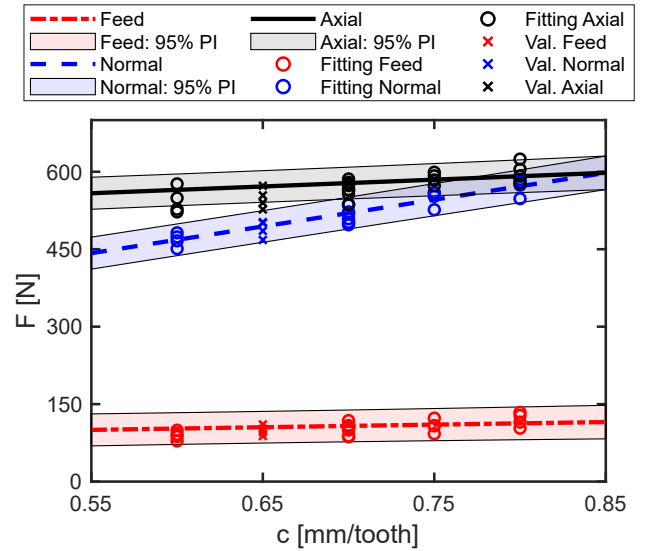

 (a) CL model: $a = 0.4 \text{ mm}$.

 (b) HF model: $a = 0.4 \text{ mm}$.

 (c) CL model: $a = 0.6 \text{ mm}$.

 (d) HF model: $a = 0.6 \text{ mm}$.

Figure 9: Mean force responses of CL and HF models versus c at the tested a values. Black solid lines represent the predicted mean axial forces, blue dashed lines describe normal forces, while red dashed-dotted lines represent feed forces. Circles represent data used for model fitting, whereas crosses represent validation data. Coloured bands represent prediction intervals of the forces components, being drawn with analogous line style and colour.

dence of the prediction. The better performance of the HF model in the prediction of this quantities lies in two main contributions: on one hand, it is related to the better estimation of the SFC; on the other hand, on the fact that the contribution to the torque of an infinitesimal piece of cutting edge is proportional to its distance from the mill axis. The second factor was in fact considered in the HF model, while it was not present in the original CL model. Furthermore, the higher confidence in the prediction of spindle torque was due just to the first of the two contributions. In fact the prediction

uncertainties were obtained from the SFC confidence intervals propagation. Being more confident on the SFC turned of course in a higher confidence in the prediction. The RM-SPE for the torques were equal to 0.33 Nm and 1.25 Nm , for the HF and CL respectively. The associated validation maximum errors (in module) were 0.44 Nm for HF and 1.61 Nm for CL. The MAPE metric relative to spindle torque underlined the improvements introduced with the HF model, assuming values of 9.7% and 34.8% for the HF and CL models, respectively. The same reasonings were valid for the spindle

power. Figures 8e and 8f represented the spindle power versus the cutting speed and the feed per tooth under $a = 0.4 \text{ mm}$ and $a = 0.6 \text{ mm}$, respectively. For the cutting power, RM-SPE resulted to be 29 W and 120 W , for the HF and CL respectively. The associated validation maximum errors (in module) were 44 W for HF and 161 W for CL. The associated MAPE values were 8.1% for HF and 32.8% for CL.

4. Conclusions

In this paper, a novel analytical mechanistic model for double-phased high-feed mills was proposed. Double-phased cutters allow to reach high feed per tooth values, while keeping a low axial depth of cut; this permits to increase the material removal rate of face-milling operations and, at the same time, to avoid cutting instability. The new formulation extended the reference literature model to include complex cutter geometry and variable engagement conditions along the axial coordinate of the tool. A longer edge contact length led to lower specific force coefficients and to the predominance of ploughing under the flank face of the cutting insert.

The developed high-feed model introduced the above improvements while keeping the formulation analytical and in closed form, both for instantaneous and mean cutting forces expressions. The model computational time remains low, relying upon neither discretization nor time integration. The model fitting procedure on mean forces takes 46.7 ms for the proposed model, whereas 12.3 ms for the literature one.

A reliable estimate of the specific force coefficients was achieved, with narrower confidence intervals with respect to the literature model, underlining a better representation of the phenomenon. Based on this, the developed model outperformed the literature one in mean forces fitting and prediction, while respecting all the regression assumptions. The same high-feed model could be used for multiple cutting conditions: low (0.4 mm) and high (0.6 mm) axial depth of cuts. The Root Mean Squared Prediction Errors were 15 N and 41 N , with associated validation maximum errors (in module) of 44 N and 79 N for the proposed and literature model, respectively.

The literature model was outperformed also in the prediction of spindle torque and power. The developed model predictions were considerably more accurate in terms of mean, reaching Root Mean Squared Prediction Errors of (0.33 Nm , 29 W), compared with (1.25 Nm , 120 W) of the literature one, respectively. The associated validation maximum errors (in module) were (0.44 Nm , 44 W) for proposed model and (1.61 Nm , 161 W) for the literature model. Narrower specific force coefficients confidence intervals translated into reduced uncertainties in the prediction of the above quantities. This allows for reliable comparisons between operations within a sustainable perspective.

Future works will regard the application of the developed

model for energetic comparison between conventional and high-feed milling, as well as its application for the monitoring and prognostics of high-feed tools.

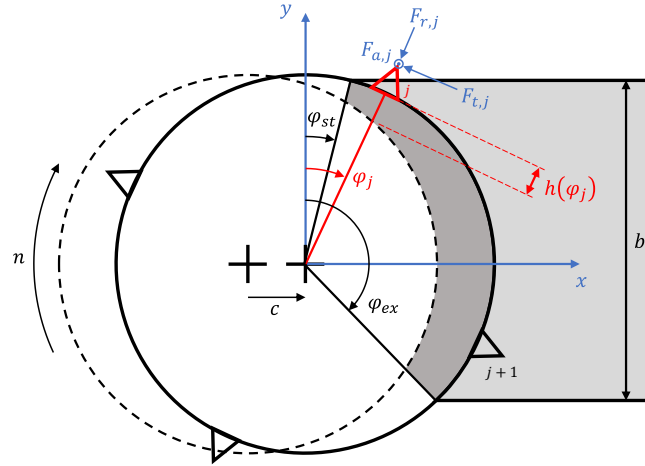


Figure A.1: Reference figure for the literature mechanistic model by Altintas. Figure represents the nomenclature of a simple milling operation: the angular position of cutters in the feed-normal reference frame, the radial engagement of the mill and the cutting forces in the cutter reference frame.

A. Theoretical background

In this appendix, the CL model developed by Altintas [21] is presented (fig. 1A-B). The tool geometry is described by the diameter of the mill D and the number of cutters N (fig. A.1). The machining process is featured by the feed per tooth c and the rotational speed n . The formulation starts by defining the position in time of the cutters as for the HF model (eq. 1). The instantaneous chip thickness removed by cutter j is approximated by equation 2, too. Two angles are defined to determine whether the j -th cutter is processing material or not: φ_{st} determines the angular position at which the cutter starts to work, φ_{ex} determines the angular position at which the cutter exits the workpiece. The engagement function is then defined (eq. A.1):

$$g(\varphi_j) = \begin{cases} 1, & \text{if } \varphi_{st} < \varphi_j < \varphi_{ex} \\ 0, & \text{otherwise.} \end{cases} \quad (\text{A.1})$$

The three components of the cutting forces (i.e. tangential, radial and axial) acting on cutter j are expressed in differential form as for the HF model (eq. 9). dA and dl are instead the infinitesimal chip area and edge contact length and are defined through (eq. A.2):

$$\begin{aligned} dA(\varphi_j) &= h(\varphi_j) dz \\ dl(\varphi_j) &= dz \end{aligned} \quad (\text{A.2})$$

Substituting equation A.2 in equation 9, and integrating in dz from 0 to the axial depth of cut a , the expressions for the three forces components are obtained:

$$\begin{aligned} F_{t,j}(\varphi_j) &= g(\varphi_j) [K_{t,c} a h(\varphi_j) + K_{t,e} a] \\ F_{r,j}(\varphi_j) &= g(\varphi_j) [K_{r,c} a h(\varphi_j) + K_{r,e} a] \\ F_{a,j}(\varphi_j) &= g(\varphi_j) [K_{a,c} a h(\varphi_j) + K_{a,e} a] \end{aligned} \quad (\text{A.3})$$

Each force term must be multiplied by $g(\varphi_j)$ to include the engagement condition in the workpiece. The force components are then projected in the feed, normal and axial direction of the milling operation, and the contribution of each cutter is summed up through equation 12.

The identification of the six SFC is based on mean cutting forces as for the HF model [62, 51]. Indeed, the three force components are integrated over one period of revolution T_P of the mill (eq. A.4):

$$\overline{F_d} = \frac{1}{T_P} \int_0^{T_P} F_d(t) dt \quad (\text{A.4})$$

where $d = x, y, z$. The resulting mean forces expressions are reported in eq. (A.5):

$$\begin{aligned}\overline{F}_x &= \frac{N a c}{8\pi} \left[K_{t,c} \cos 2\varphi - K_{r,c} (2\varphi - \sin 2\varphi) \right] \Big|_{\varphi_{st}}^{\varphi_{ex}} + \\ &\quad + \frac{N a}{2\pi} \left(-K_{t,e} \sin \varphi + K_{r,e} \cos \varphi \right) \Big|_{\varphi_{st}}^{\varphi_{ex}} \\ \overline{F}_y &= \frac{N a c}{8\pi} \left[K_{t,c} (2\varphi - \sin 2\varphi) + K_{r,c} \cos 2\varphi \right] \Big|_{\varphi_{st}}^{\varphi_{ex}} + \\ &\quad - \frac{N a}{2\pi} \left(K_{t,e} \cos \varphi + K_{r,e} \sin \varphi \right) \Big|_{\varphi_{st}}^{\varphi_{ex}} \\ \overline{F}_z &= \frac{N a}{2\pi} \left(-K_{a,c} c \cos \varphi + K_{a,c} \varphi \right) \Big|_{\varphi_{st}}^{\varphi_{ex}}\end{aligned}\tag{A.5}$$

Equation A.5 represents the mean cutting forces according to the CL model. Cutting torque T is defined in an instantaneous fashion through equation A.6:

$$T(t) = \frac{D}{2} \sum_{j=1}^N F_{t,j}(t)\tag{A.6}$$

Cutting power P is instead (eq. A.7):

$$P(t) = 2\pi n T(t)\tag{A.7}$$

B. Mathematical computations: instantaneous forces terms

Equation 11 included three terms that were not expanded in the body of the paper, due to clarity issues. The scope of this appendix is to provide the mathematical expressions and derivations of such terms. The terms that are needed for the computation of the instantaneous forces in equation 11 are $A_{int}(\varphi_j)$, $A_{ext}(\varphi_j)$ and $l(\varphi_j)$. Since the formulation does not depend on the cutter index j , such index will be omitted in the next formulas.

B.1. Undeformed internal chip area $A_{int}(\varphi)$

This term corresponds to the area underneath the previous cutter position graph in radial-axial chart. The reference graph is shown in figure B.1. The two cases represent the condition whether $a \leq z_3$ (fig. B.1a) or $a > z_3$ (fig. B.1b). This distinction is needed since it determines whether the second-phase of the cutter is engaged or not. In case $a \leq z_3$, $A_{int}(\varphi)$ can be expressed as a sum of areas of triangles and trapezoids:

$$A_{int}(\varphi) = \begin{cases} 0 & \text{if } 0 \leq \varphi \leq \varphi_{2,int} \\ \frac{1}{2} \frac{[r_\varphi(\varphi) - r_2 + h(\varphi)]^2}{r_3 - r_2} z_3 & \text{if } \varphi_{2,int} < \varphi \leq \varphi_{a,int} \\ \frac{1}{2} a [r_{a,int}(\varphi) - r_2 + h(\varphi)] + a [r_\varphi(\varphi) - r_{a,int}(\varphi)] & \text{if } \varphi_{a,int} < \varphi \leq \varphi_{a,ext} \\ \frac{1}{2} a [r_{a,int}(\varphi) - r_2 + h(\varphi)] + a [r_{a,ext} - r_{a,int}(\varphi)] & \text{if } \varphi_{a,ext} < \varphi \leq \pi \\ 0 & \text{if } \pi < \varphi < 2\pi \end{cases}\tag{B.1}$$

Instead, if $a > z_3$, the formulation becomes:

$$A_{int}(\varphi) = \begin{cases} 0, & \text{if } 0 \leq \varphi \leq \varphi_{2,int} \\ \frac{1}{2} \frac{[r_\varphi(\varphi) - r_2 + h(\varphi)]^2}{r_3 - r_2} z_3, & \text{if } \varphi_{2,int} < \varphi \leq \varphi_{3,int} \\ \frac{1}{2} (r_3 - r_2) z_3 + [r_\varphi(\varphi) - r_3 + h(\varphi)] z_3 + \frac{1}{2} [r_\varphi(\varphi) - r_3 + h(\varphi)]^2 \frac{z_4 - z_3}{r_4 - r_3}, & \text{if } \varphi_{3,int} < \varphi \leq \varphi_{a,int} \\ \frac{1}{2} (r_3 - r_2) z_3 + \frac{1}{2} (z_3 + a) [r_{a,int}(\varphi) - r_3 + h(\varphi)] + a [r_\varphi(\varphi) - r_{a,int}(\varphi)], & \text{if } \varphi_{a,int} < \varphi \leq \varphi_{a,ext} \\ \frac{1}{2} (r_3 - r_2) z_3 + \frac{1}{2} (z_3 + a) [r_{a,int}(\varphi) - r_3 + h(\varphi)] + a [r_{a,ext} - r_{a,int}(\varphi)], & \text{if } \varphi_{a,ext} < \varphi \leq \pi \\ 0, & \text{if } \pi < \varphi < 2\pi \end{cases}\tag{B.2}$$

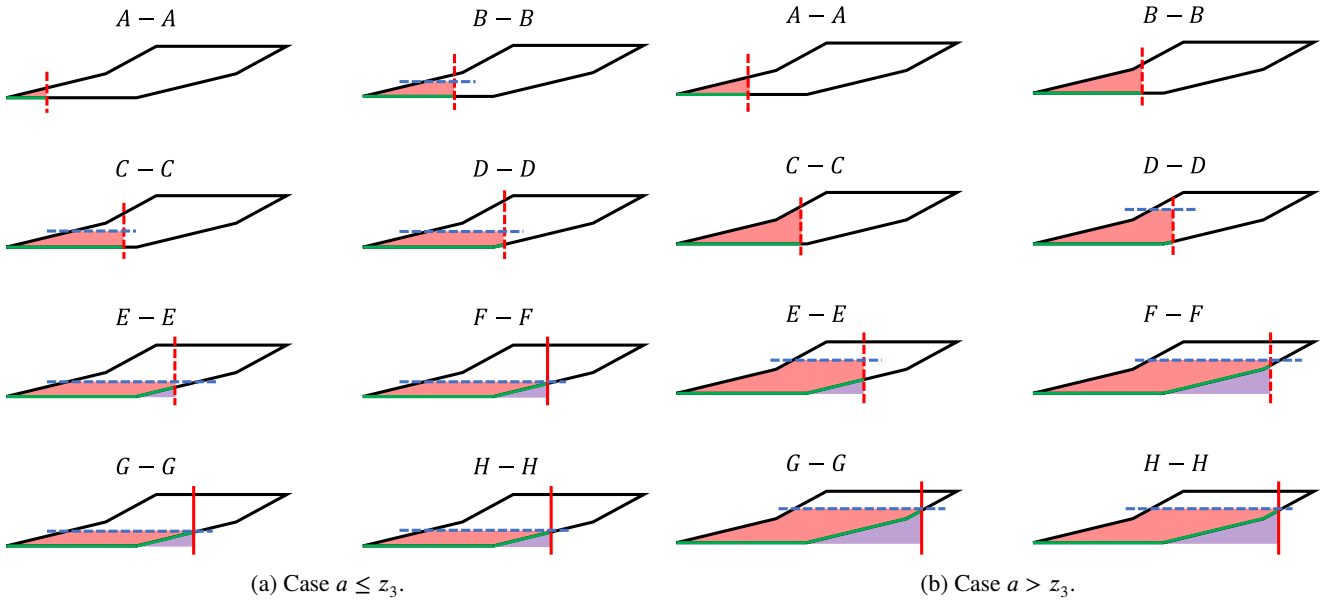


Figure B.1: Representation of the main quantities defining the chip shape. The red area is $A_{int}(\varphi)$; violet area is the superimposition of $A_{int}(\varphi)$ and $A_{ext}(\varphi)$; green solid line is $l(\varphi)$; red dashed line is $r_\varphi(\varphi)$ and red solid line is $r_\varphi(\varphi) = r_{a,ext}$; blue dashed line represents the axial depth of cut limit.

B.2. Undeformed external chip area $A_{ext}(\varphi)$

The same cases are also valid for $A_{ext}(\varphi)$, which represents the area under the graph of the current insert cutting edge in the radial-axial chart. Figures B.1a and B.1b are again the references. In case $a \leq z_3$, $A_{ext}(\varphi)$ is:

$$A_{ext}(\varphi) = \begin{cases} 0, & \text{if } 0 \leq \varphi \leq \varphi_{2,ext} \\ \frac{1}{2} \frac{[r_\varphi(\varphi) - r_2]^2}{r_3 - r_2} z_3, & \text{if } \varphi_{2,ext} < \varphi \leq \varphi_{a,ext} \\ \frac{1}{2} a (r_{a,ext} - r_2), & \text{if } \varphi_{a,ext} < \varphi \leq \pi \\ 0, & \text{if } \pi < \varphi < 2\pi \end{cases} \quad (\text{B.3})$$

Instead, if $a > z_3$, the formulation becomes:

$$A_{ext}(\varphi) = \begin{cases} 0, & \text{if } 0 \leq \varphi \leq \varphi_{2,ext} \\ \frac{1}{2} \frac{[r_\varphi(\varphi) - r_2]^2}{r_3 - r_2} z_3, & \text{if } \varphi_{2,ext} < \varphi \leq \varphi_{3,ext} \\ \frac{1}{2} z_3 (r_3 - r_2) + z_3 [r_\varphi(\varphi) - r_3] + \frac{1}{2} (z_4 - z_3) \frac{[r_\varphi(\varphi) - r_3]^2}{r_4 - r_3}, & \text{if } \varphi_{3,ext} < \varphi \leq \varphi_{a,ext} \\ \frac{1}{2} z_3 (r_3 - r_2) + \frac{1}{2} (z_3 + a) (r_{a,ext} - r_3), & \text{if } \varphi_{a,ext} < \varphi \leq \pi \\ 0, & \text{if } \pi < \varphi < 2\pi \end{cases} \quad (\text{B.4})$$

B.3. Edge contact length $l(\varphi)$

This term represents the length of the cutting edge which is involved in the cut of the chip. It is the length of the engaged part of the actual cutter. The same computations as before are done also for $l(\varphi)$ (fig. B.1a and B.1b). Here, a supplementary term is added to the integral, which is the minor cutting edge contribution. The resultant formulas for $a \leq z_3$ are:

$$l(\varphi) = \begin{cases} 0, & \text{if } 0 \leq \varphi \leq \varphi_{2,int} \\ r_\varphi(\varphi) - r_2 + h(\varphi), & \text{if } \varphi_{2,int} \leq \varphi \leq \varphi_{2,ext} \\ h(\varphi) + [r_\varphi(\varphi) - r_2] \sqrt{1 + \left(\frac{z_3}{r_3 - r_2}\right)^2}, & \text{if } \varphi_{2,ext} \leq \varphi \leq \varphi_{a,ext} \\ h(\varphi) + \sqrt{(r_{a,ext} - r_2)^2 + a^2}, & \text{if } \varphi_{a,ext} \leq \varphi \leq \pi \\ 0, & \text{if } \pi < \varphi < 2\pi \end{cases} \quad (\text{B.5})$$

In case $a > z_3$:

$$l(\varphi) = \begin{cases} 0, & \text{if } 0 \leq \varphi \leq \varphi_{2,int} \\ r_\varphi(\varphi) - r_2 + h(\varphi), & \text{if } \varphi_{2,int} \leq \varphi \leq \varphi_{2,ext} \\ h(\varphi) + [r_\varphi(\varphi) - r_2] \sqrt{1 + \left(\frac{z_3}{r_3 - r_2}\right)^2}, & \text{if } \varphi_{2,ext} \leq \varphi \leq \varphi_{3,ext} \\ h(\varphi) + \sqrt{(r_3 - r_2)^2 + z_3^2} + [r_\varphi(\varphi) - r_3] \sqrt{1 + \left(\frac{z_4 - z_3}{r_4 - r_3}\right)^2}, & \text{if } \varphi_{3,ext} \leq \varphi \leq \varphi_{a,ext} \\ h(\varphi) + \sqrt{(r_3 - r_2)^2 + z_3^2} + \sqrt{(r_{a,ext} - r_3)^2 + (a - z_3)^2}, & \text{if } \varphi_{a,ext} \leq \varphi \leq \pi \\ 0, & \text{if } \pi < \varphi < 2\pi \end{cases} \quad (\text{B.6})$$

B.4. Torque area equivalent radius $r_A^*(\varphi)$

Furthermore, two more quantities need to be expressed for equation 15. The first one is $r_A^*(\varphi)$. Starting with case $a \leq z_3$:

$$r_{A,int}^*(\varphi) = \begin{cases} 0, & \text{if } 0 \leq \varphi \leq \varphi_{2,int} \\ r_2 - h(\varphi) + \frac{2[r_\varphi(\varphi) - r_2 + h(\varphi)]}{3}, & \text{if } \varphi_{2,int} < \varphi \leq \varphi_{a,int} \\ \frac{1}{A_{int}(\varphi)} \left\{ \left[r_2 - h(\varphi) + \frac{2(r_{a,int}(\varphi) - r_2 + h(\varphi))}{3} \right] \frac{a[r_{a,int}(\varphi) - r_2 + h(\varphi)]}{2} + \right. \\ \left. + \frac{[r_\varphi(\varphi) + r_{a,int}(\varphi)]a[r_\varphi(\varphi) - r_{a,int}(\varphi)]}{2} \right\}, & \text{if } \varphi_{a,int} < \varphi \leq \varphi_{a,ext} \\ \frac{1}{A_{int}(\varphi)} \left\{ \left[r_2 - h(\varphi) + \frac{2(r_{a,int}(\varphi) - r_2 + h(\varphi))}{3} \right] \frac{a[r_{a,int}(\varphi) - r_2 + h(\varphi)]}{2} + \right. \\ \left. + \frac{[r_{a,ext} + r_{a,int}(\varphi)]a[r_{a,ext} - r_{a,int}(\varphi)]}{2} \right\}, & \text{if } \varphi_{a,ext} < \varphi \leq \pi \\ 0, & \text{if } \pi < \varphi < 2\pi \end{cases} \quad (\text{B.7})$$

$$r_{A,ext}^*(\varphi) = \begin{cases} 0, & \text{if } 0 \leq \varphi \leq \varphi_{2,ext} \\ r_2 + \frac{2[r_\varphi(\varphi) - r_2]}{3}, & \text{if } \varphi_{2,ext} < \varphi \leq \varphi_{a,ext} \\ r_2 + \frac{2 \cdot (r_{a,ext} - r_2)}{3}, & \text{if } \varphi_{a,ext} < \varphi \leq \pi \\ 0, & \text{if } \pi < \varphi < 2\pi \end{cases}$$

$$r_A^*(\varphi) = \begin{cases} \frac{r_{A,int}^*(\varphi) \cdot A_{int}(\varphi) - r_{A,ext}^*(\varphi) \cdot A_{ext}(\varphi)}{A_{int}(\varphi) - A_{ext}(\varphi)}, & \text{if } A_{int}(\varphi) - A_{ext}(\varphi) \neq 0 \\ 0, & \text{if } A_{int}(\varphi) - A_{ext}(\varphi) = 0 \end{cases}$$

While in case $a > z_3$, it is defined as follows:

$$r_{A,int}^*(\varphi) = \begin{cases} 0, & \text{if } 0 \leq \varphi \leq \varphi_{2,int} \\ r_2 - h(\varphi) + \frac{2[r_\varphi(\varphi) - r_2 + h(\varphi)]}{3}, & \text{if } \varphi_{2,int} < \varphi \leq \varphi_{3,int} \\ \frac{1}{A_{int}(\varphi)} \left\{ \left[r_2 - h(\varphi) + \frac{2(r_3 - r_2)}{3} \right] \frac{(r_3 - r_2)z_3}{2} + \frac{[r_3 - h(\varphi) + r_\varphi(\varphi)][r_\varphi(\varphi) - r_3 + h(\varphi)]z_3}{2} + \right. \\ \left. + \left[r_3 - h(\varphi) + \frac{2(r_\varphi(\varphi) - r_3 + h(\varphi))}{3} \right] \frac{(z_4 - z_3)[r_\varphi(\varphi) - r_3 + h(\varphi)]^2}{2(r_4 - r_3)} \right\}, & \text{if } \varphi_{3,int} < \varphi \leq \varphi_{a,int} \\ \frac{1}{A_{int}(\varphi)} \left\{ \left[r_2 - h(\varphi) + \frac{2(r_3 - r_2)}{3} \right] \frac{(r_3 - r_2)z_3}{2} + \frac{[r_3 - h(\varphi) + r_{a,int}(\varphi)][r_{a,int}(\varphi) - r_3 + h(\varphi)]z_3}{2} + \right. \\ \left. + \left[r_3 - h(\varphi) + \frac{2(r_{a,int}(\varphi) - r_3 + h(\varphi))}{3} \right] \frac{(a - z_3)[r_{a,int}(\varphi) - r_3 + h(\varphi)]}{2} + \right. \\ \left. + \frac{[r_{a,int}(\varphi) + r_\varphi(\varphi)][r_\varphi(\varphi) - r_{a,int}(\varphi)]a}{2} \right\}, & \text{if } \varphi_{a,int} < \varphi \leq \varphi_{a,ext} \\ \frac{1}{A_{int}(\varphi)} \left\{ \left[r_2 - h(\varphi) + \frac{2(r_3 - r_2)}{3} \right] \frac{(r_3 - r_2)z_3}{2} + \frac{[r_3 - h(\varphi) + r_{a,int}(\varphi)][r_{a,int}(\varphi) - r_3 + h(\varphi)]z_3}{2} + \right. \\ \left. + \left[r_3 - h(\varphi) + \frac{2(r_{a,int}(\varphi) - r_3 + h(\varphi))}{3} \right] \frac{(a - z_3)[r_{a,int}(\varphi) - r_3 + h(\varphi)]}{2} + \right. \\ \left. + \frac{[r_{a,int}(\varphi) + r_{a,ext}][r_{a,ext} - r_{a,int}(\varphi)]a}{2} \right\}, & \text{if } \varphi_{a,ext} < \varphi \leq \pi \\ 0, & \text{if } \pi < \varphi < 2\pi \end{cases} \quad (\text{B.8})$$

$$r_{A,ext}^*(\varphi) = \begin{cases} 0, & \text{if } 0 \leq \varphi \leq \varphi_{2,ext} \\ r_2 + \frac{2[r_\varphi(\varphi) - r_2]}{3}, & \text{if } \varphi_{2,ext} < \varphi \leq \varphi_{3,ext} \\ \frac{1}{A_{ext}(\varphi)} \left\{ \left[r_2 + \frac{2(r_3 - r_2)}{3} \right] \left[\frac{z_3(r_3 - r_2)}{2} \right] + \frac{z_3[r_\varphi(\varphi) + r_3][r_\varphi(\varphi) - r_3]}{2} + \right. \\ \left. + \left[r_3 + \frac{2(r_\varphi(\varphi) - r_3)}{3} \right] \frac{(z_4 - z_3)[r_\varphi(\varphi) - r_3]^2}{2(r_4 - r_3)} \right\}, & \text{if } \varphi_{3,ext} < \varphi \leq \varphi_{a,ext} \\ \frac{1}{A_{ext}(\varphi)} \left\{ \left[r_2 + \frac{2(r_3 - r_2)}{3} \right] \left[\frac{z_3(r_3 - r_2)}{2} \right] + \frac{z_3(r_{a,ext} + r_3)(r_{a,ext} - r_3)}{2} + \right. \\ \left. + \left[r_3 + \frac{2(r_{a,ext} - r_3)}{3} \right] \frac{(z_4 - z_3)(r_{a,ext} - r_3)^2}{2(r_4 - r_3)} \right\}, & \text{if } \varphi_{a,ext} < \varphi \leq \pi \\ 0, & \text{if } \pi < \varphi < 2\pi \end{cases}$$

$$r_A^*(\varphi) = \begin{cases} \frac{r_{A,int}^*(\varphi) \cdot A_{int}(\varphi) - r_{A,ext}^*(\varphi) \cdot A_{ext}(\varphi)}{A_{int}(\varphi) - A_{ext}(\varphi)}, & \text{if } A_{int}(\varphi) - A_{ext}(\varphi) \neq 0 \\ 0, & \text{if } A_{int}(\varphi) - A_{ext}(\varphi) = 0 \end{cases}$$

B.5. Torque edge contact length equivalent radius $r_l^*(\varphi)$

The second term that needs to be expressed for equation 15 is $r_l^*(\varphi)$. In case $a \leq z_3$, this term is equal to:

$$r_l^*(\varphi) = \begin{cases} 0, & \text{if } 0 \leq \varphi \leq \varphi_{2,int} \\ \frac{r_\varphi(\varphi)+r_2-h(\varphi)}{2}, & \text{if } \varphi_{2,int} \leq \varphi \leq \varphi_{2,ext} \\ \frac{1}{l(\varphi)} \left\{ \left[r_2 - \frac{h(\varphi)}{2} \right] h(\varphi) + \frac{[r_\varphi(\varphi)+r_2][r_\varphi(\varphi)-r_2]}{2} \sqrt{1 + \left(\frac{z_3}{r_3-r_2} \right)^2} \right\}, & \text{if } \varphi_{2,ext} \leq \varphi \leq \varphi_{a,ext} \\ \frac{1}{l(\varphi)} \left\{ \left[r_2 - \frac{h(\varphi)}{2} \right] h(\varphi) + \frac{r_{a,ext}+r_2}{2} \sqrt{a^2 + (r_{a,ext} - r_2)^2} \right\}, & \text{if } \varphi_{a,ext} \leq \varphi \leq \pi \\ 0, & \text{if } \pi < \varphi < 2\pi \end{cases} \quad (\text{B.9})$$

In case $a > z_3$:

$$r_l^*(\varphi) = \begin{cases} 0, & \text{if } 0 \leq \varphi \leq \varphi_{2,int} \\ \frac{r_\varphi(\varphi)+r_2-h(\varphi)}{2}, & \text{if } \varphi_{2,int} \leq \varphi \leq \varphi_{2,ext} \\ \frac{1}{l(\varphi)} \left\{ \left[r_2 - \frac{h(\varphi)}{2} \right] h(\varphi) + \frac{[r_\varphi(\varphi)+r_2][r_\varphi(\varphi)-r_2]}{2} \sqrt{1 + \left(\frac{z_3}{r_3-r_2} \right)^2} \right\}, & \text{if } \varphi_{2,ext} \leq \varphi \leq \varphi_{3,ext} \\ \frac{1}{l(\varphi)} \left\{ \left[r_2 - \frac{h(\varphi)}{2} \right] h(\varphi) + \frac{(r_3+r_2)(r_3-r_2)}{2} \sqrt{1 + \left(\frac{z_3}{r_3-r_2} \right)^2} + \right. & \text{if } \varphi_{3,ext} \leq \varphi \leq \varphi_{a,ext} \\ \quad \left. + \frac{[r_\varphi(\varphi)+r_3][r_\varphi(\varphi)-r_3]}{2} \sqrt{1 + \left(\frac{z_4-z_3}{r_4-r_3} \right)^2} \right\}, & \\ \frac{1}{l(\varphi)} \left\{ \left[r_2 - \frac{h(\varphi)}{2} \right] h(\varphi) + \frac{(r_3+r_2)(r_3-r_2)}{2} \sqrt{1 + \left(\frac{z_3}{r_3-r_2} \right)^2} + \right. & \text{if } \varphi_{a,ext} \leq \varphi \leq \pi \\ \quad \left. + \frac{(r_{a,ext}+r_3)(r_{a,ext}-r_3)}{2} \sqrt{1 + \left(\frac{z_4-z_3}{r_4-r_3} \right)^2} \right\}, & \\ 0, & \text{if } \pi < \varphi < 2\pi \end{cases} \quad (\text{B.10})$$

C. Mathematical computations: mean forces terms

Equation 13 presented ten terms which were not presented due to space issues. The goal of this appendix is to present the formulation of each term. Actually, only a subset of these terms must be defined, in fact some relationships can be found:

$$\begin{aligned} a_{11} &= \int_0^{2\pi} [A_{int}(\varphi) - A_{ext}(\varphi)] \cos \varphi \, d\varphi & a_{22} &= \int_0^{2\pi} l(\varphi) \sin \varphi \, d\varphi = a_{14} \\ a_{12} &= \int_0^{2\pi} l(\varphi) \cos \varphi \, d\varphi & a_{23} &= \int_0^{2\pi} [A_{int}(\varphi) - A_{ext}(\varphi)] \cos \varphi \, d\varphi = a_{11} \\ a_{13} &= \int_0^{2\pi} [A_{int}(\varphi) - A_{ext}(\varphi)] \sin \varphi \, d\varphi & a_{24} &= \int_0^{2\pi} l(\varphi) \cos \varphi \, d\varphi = a_{12} \\ a_{14} &= \int_0^{2\pi} l(\varphi) \sin \varphi \, d\varphi & a_{35} &= \int_0^{2\pi} [A_{int}(\varphi) - A_{ext}(\varphi)] \, d\varphi \\ a_{21} &= \int_0^{2\pi} [A_{int}(\varphi) - A_{ext}(\varphi)] \sin \varphi \, d\varphi = a_{13} & a_{36} &= \int_0^{2\pi} l(\varphi) \, d\varphi \end{aligned} \quad (\text{C.1})$$

This means that only six terms are independent and need to be computed. Each term was computed for the two cases $a \leq z_3$ and $a > z_3$.

C.1. The case of $a \leq z_3$

For the sake of clarity, the derivation was presented just for the first terms. For the area terms, the integral was split into two parts, one related to the internal profile and one to the external profile. These terms were referred with $a_{do,A}$ and $a_{do,B}$ respectively. Starting from a_{11} , substituting equations B.1 and B.3 in the integral and splitting it, it follows:

$$\begin{aligned}
 a_{11,A} &= \int_{\varphi_{2,int}}^{\varphi_{a,int}} \frac{[r_\varphi(\varphi) - r_2 + c \sin \varphi]^2 z_3 \cos \varphi}{2(r_3 - r_2)} d\varphi + \int_{\varphi_{a,int}}^{\varphi_{a,ext}} \left\{ \frac{a[r_{a,int}(\varphi) - r_2 + c \sin \varphi]}{2} + \right. \\
 &\quad \left. + a[r_\varphi(\varphi) - r_{a,int}(\varphi)] \right\} \cos \varphi d\varphi + \int_{\varphi_{a,ext}}^{\pi} \left\{ \frac{a[r_{a,int}(\varphi) - r_2 + c \sin \varphi]}{2} + a[r_{a,ext} - r_{a,int}(\varphi)] \right\} \cos \varphi d\varphi = \\
 &= \left\{ \frac{z_3(b - r_{nom})^2}{2(r_3 - r_2)} \ln \frac{1 + \sin \varphi}{\cos \varphi} + \frac{z_3 r_2^2 \sin \varphi}{2(r_3 - r_2)} + \frac{z_3 c^2 \sin^3 \varphi}{6(r_3 - r_2)} - \frac{z_3 r_2(b - r_{nom}) \varphi}{r_3 - r_2} + \right. \\
 &\quad \left. - \frac{z_3 c(b - r_{nom}) \cos \varphi}{r_3 - r_2} - \frac{z_3 r_2 c \sin^2 \varphi}{2(r_3 - r_2)} \right\} \Big|_{\varphi_{2,int}}^{\varphi_{a,int}} + \left\{ \frac{a(r_{a,ext} - r_2) \sin \varphi}{2} + (b - r_{nom}) a \varphi + \right. \\
 &\quad \left. - a r_{a,ext} \sin \varphi + \frac{c a \sin^2 \varphi}{2} \right\} \Big|_{\varphi_{a,int}}^{\varphi_{a,ext}} + \left\{ \frac{a(r_{a,ext} - r_2) \sin \varphi}{2} + \frac{c a \sin^2 \varphi}{2} \right\} \Big|_{\varphi_{a,ext}}^{\pi} \quad (C.2)
 \end{aligned}$$

$$\begin{aligned}
 a_{11,B} &= \int_{\varphi_{2,ext}}^{\varphi_{a,ext}} \frac{[r_\varphi(\varphi) - r_2]^2 z_3 \cos \varphi}{2(r_3 - r_2)} d\varphi + \int_{\varphi_{a,ext}}^{\pi} \frac{r_{a,ext} a \cos \varphi}{2} d\varphi = \\
 &= \left\{ \frac{z_3(b - r_{nom})^2}{2(r_3 - r_2)} \ln \frac{1 + \sin \varphi}{\cos \varphi} + \frac{r_2^2 z_3 \sin \varphi}{2(r_3 - r_2)} - \frac{r_2 z_3(b - r_{nom}) \varphi}{r_3 - r_2} \right\} \Big|_{\varphi_{2,ext}}^{\varphi_{a,ext}} + \\
 &\quad + \left\{ \frac{(r_{a,ext} - r_2) a \sin \varphi}{2} \right\} \Big|_{\varphi_{a,ext}}^{\pi}
 \end{aligned}$$

$$a_{11} = a_{23} = a_{11,A} - a_{11,B}$$

The second term is instead solved in the following:

$$\begin{aligned}
 a_{12} &= \int_{\varphi_{2,int}}^{\varphi_{2,ext}} [r_\varphi(\varphi) - r_2 + c \sin \varphi] \cos \varphi d\varphi + \int_{\varphi_{2,ext}}^{\varphi_{a,ext}} \left\{ c \sin \varphi + [r_\varphi(\varphi) - r_2] \sqrt{1 + \left(\frac{z_3}{r_3 - r_2} \right)^2} \right\} \cos \varphi d\varphi + \\
 &\quad + \int_{\varphi_{a,ext}}^{\pi} \left[c \sin \varphi + \sqrt{(r_{a,ext} - r_2)^2 + a^2} \right] \cos \varphi d\varphi = \\
 &= \left\{ (b - r_{nom}) \varphi - r_2 \sin \varphi + \frac{c \sin^2 \varphi}{2} \right\} \Big|_{\varphi_{2,int}}^{\varphi_{2,ext}} + \left\{ \frac{c \sin^2 \varphi}{2} + (b - r_{nom}) \sqrt{1 + \left(\frac{z_3}{r_3 - r_2} \right)^2} \varphi + \right. \\
 &\quad \left. - r_2 \sqrt{1 + \left(\frac{z_3}{r_3 - r_2} \right)^2} \sin \varphi \right\} \Big|_{\varphi_{2,ext}}^{\varphi_{a,ext}} + \left\{ \frac{c \sin^2 \varphi}{2} + \sqrt{(r_{a,ext} - r_2)^2 + a^2} \sin \varphi \right\} \Big|_{\varphi_{a,ext}}^{\pi} \quad (C.3)
 \end{aligned}$$

$$a_{12} = a_{24}$$

The third term is expressed as follows:

$$\begin{aligned}
 a_{13,A} = & \left\{ \frac{z_3 (b - r_{nom})^2}{2 (r_3 - r_2) \cos \varphi} - \frac{z_3 r_2^2 \cos \varphi}{2 (r_3 - r_2)} + \frac{c^2 z_3 \cos \varphi (\cos^2 \varphi - 3)}{6 (r_3 - r_2)} + \frac{z_3 r_2 (b - r_{nom}) \ln \cos \varphi}{r_3 - r_2} + \right. \\
 & - \frac{z_3 c r_2}{r_3 - r_2} \left(\frac{\varphi}{2} - \frac{\sin 2\varphi}{4} \right) + \frac{z_3 c (b - r_{nom})}{r_3 - r_2} \left[\ln \tan \left(\frac{\varphi}{2} + \frac{\pi}{4} \right) - \sin \varphi \right] \Big|_{\varphi_{2,int}}^{\varphi_{a,int}} + \left\{ -\frac{a (r_{a,ext} - r_2) \cos \varphi}{2} + \right. \\
 & - a (b - r_{nom}) \ln \cos \varphi + a r_{a,ext} \cos \varphi + a c \left(\frac{\varphi}{2} - \frac{\sin 2\varphi}{4} \right) \Big|_{\varphi_{a,int}}^{\varphi_{a,ext}} + \left\{ -\frac{a (r_{a,ext} - r_2) \cos \varphi}{2} + \right. \\
 & \left. \left. + a c \left(\frac{\varphi}{2} - \frac{\sin 2\varphi}{4} \right) \right\} \Big|_{\varphi_{a,ext}}^{\pi} \right. \quad (C.4)
 \end{aligned}$$

$$a_{13,B} = \left\{ \frac{z_3 (b - r_{nom})^2}{2 (r_3 - r_2) \cos \varphi} - \frac{r_2^2 z_3 \cos \varphi}{2 (r_3 - r_2)} + \frac{r_2 z_3 (b - r_{nom}) \ln \cos \varphi}{r_3 - r_2} \right\} \Big|_{\varphi_{2,ext}}^{\varphi_{a,ext}} + \left\{ -\frac{(r_{a,ext} - r_2) a \cos \varphi}{2} \right\} \Big|_{\varphi_{a,ext}}^{\pi}$$

$$a_{13} = a_{21} = a_{13,A} - a_{13,B}$$

The fourth term is then presented:

$$\begin{aligned}
 a_{14} = & \left\{ - (b - r_{nom}) \ln \cos \varphi + r_2 \cos \varphi + c \left(\frac{\varphi}{2} - \frac{\sin 2\varphi}{4} \right) \right\} \Big|_{\varphi_{2,int}}^{\varphi_{2,ext}} + \left\{ c \left(\frac{\varphi}{2} - \frac{\sin 2\varphi}{4} \right) + \right. \\
 & - (b - r_{nom}) \sqrt{1 + \left(\frac{z_3}{r_3 - r_2} \right)^2} \ln \cos \varphi + r_2 \sqrt{1 + \left(\frac{z_3}{r_3 - r_2} \right)^2} \cos \varphi \Big|_{\varphi_{2,ext}}^{\varphi_{a,ext}} + \left\{ c \left(\frac{\varphi}{2} - \frac{\sin 2\varphi}{4} \right) + \right. \\
 & \left. - \sqrt{(r_{a,ext} - r_2)^2 + a^2} \cos \varphi \right\} \Big|_{\varphi_{a,ext}}^{\pi} \quad (C.5)
 \end{aligned}$$

$$a_{14} = a_{22}$$

The fifth term is reported in the following:

$$\begin{aligned}
 a_{35,A} = & \left\{ \frac{z_3}{2 (r_3 - r_2)} \left[(b - r_{nom})^2 \tan \varphi + r_2^2 \varphi + \frac{c^2 \varphi}{2} - \frac{c^2 \sin 2\varphi}{4} - 2 r_2 (b - r_{nom}) \ln (\tan \varphi + \sec \varphi) + \right. \right. \\
 & \left. - 2 c (b - r_{nom}) \ln \cos \varphi + 2 r_2 c \cos \varphi \right] \Big|_{\varphi_{2,int}}^{\varphi_{a,int}} + \left\{ \frac{a (r_{a,ext} - r_2) \varphi}{2} + a (b - r_{nom}) \ln (\tan \varphi + \sec \varphi) + \right. \\
 & \left. - a r_{a,ext} \varphi - a c \cos \varphi \right\} \Big|_{\varphi_{a,int}}^{\varphi_{a,ext}} + \left\{ \frac{a (r_{a,ext} - r_2) \varphi}{2} - a c \cos \varphi \right\} \Big|_{\varphi_{a,ext}}^{\pi} \quad (C.6)
 \end{aligned}$$

$$\begin{aligned}
 a_{35,B} = & \left\{ \frac{z_3}{2 (r_3 - r_2)} \left[(b - r_{nom})^2 \tan \varphi + r_2^2 \varphi - 2 r_2 (b - r_{nom}) \ln (\tan \varphi + \sec \varphi) \right] \right\} \Big|_{\varphi_{2,ext}}^{\varphi_{a,ext}} + \\
 & + \left\{ \frac{(r_{a,ext} - r_2) a \varphi}{2} \right\} \Big|_{\varphi_{a,ext}}^{\pi}
 \end{aligned}$$

$$a_{35} = a_{35,A} - a_{35,B}$$

The last term is expressed as in the following:

$$\begin{aligned}
 a_{36} = & \left\{ (b - r_{nom}) \ln(\tan \varphi + \sec \varphi) - r_2 \varphi - c \cos \varphi \right\} \Big|_{\varphi_{2,int}}^{\varphi_{2,ext}} + \left\{ -c \cos \varphi + \right. \\
 & + \sqrt{1 + \left(\frac{z_3}{r_3 - r_2} \right)^2} \left[(b - r_{nom}) \ln(\tan \varphi + \sec \varphi) - r_2 \varphi \right] \Big|_{\varphi_{2,ext}}^{\varphi_{a,ext}} + \left\{ -c \cos \varphi + \right. \\
 & \left. + \sqrt{(r_{a,ext} - r_2)^2 + a^2} \varphi \right\} \Big|_{\varphi_{a,ext}}^{\pi}
 \end{aligned} \quad (C.7)$$

C.2. The case of $a > z_3$

All the computations performed for the $a \leq z_3$ case were carried out using the definitions of $A_{int}(\varphi)$, $A_{ext}(\varphi)$ and $I(\varphi)$ in the $a > z_3$ case, producing different formulations for the ten terms of equation 13. Starting from a_{11} , substituting equations B.2 and B.4 in the integral and splitting it, it follows:

$$\begin{aligned}
 a_{11,A} = & \left\{ \frac{z_3 (b - r_{nom})^2}{2 (r_3 - r_2)} \ln \frac{1 + \sin \varphi}{\cos \varphi} + \frac{r_2^2 z_3 \sin \varphi}{2 (r_3 - r_2)} + \frac{z_3 c^2 \sin^3 \varphi}{6 (r_3 - r_2)} - \frac{r_2 (b - r_{nom}) z_3 \varphi}{r_3 - r_2} + \right. \\
 & - \frac{z_3 c (b - r_{nom}) \cos \varphi}{r_3 - r_2} - \frac{z_3 r_2 c \sin^2 \varphi}{2 (r_3 - r_2)} \Big\} \Big|_{\varphi_{2,int}}^{\varphi_{3,int}} + \left\{ \frac{(r_3 - r_2) z_3 \sin \varphi}{2} + z_3 (b - r_{nom}) \varphi + \right. \\
 & - z_3 r_3 \sin \varphi + \frac{c z_3 \sin^2 \varphi}{2} + \frac{(z_4 - z_3) (b - r_{nom})^2}{2 (r_4 - r_3)} \ln \frac{1 + \sin \varphi}{\cos \varphi} + \frac{r_3^2 (z_4 - z_3) \sin \varphi}{2 (r_4 - r_3)} + \\
 & + \frac{(z_4 - z_3) c^2 \sin^3 \varphi}{6 (r_4 - r_3)} - \frac{(z_4 - z_3) (b - r_{nom}) r_3 \varphi}{r_4 - r_3} - \frac{r_3 c (z_4 - z_3) \sin^2 \varphi}{2 (r_4 - r_3)} + \\
 & - \frac{c (b - r_{nom}) (z_4 - z_3) \cos \varphi}{r_4 - r_3} \Big\} \Big|_{\varphi_{3,int}}^{\varphi_{a,int}} + \left\{ \frac{(r_3 - r_2) z_3 \sin \varphi}{2} + \frac{(z_3 + a) (r_{a,ext} - r_3) \sin \varphi}{2} + \right. \\
 & + a (b - r_{nom}) \varphi - a r_{a,ext} \sin \varphi + \frac{a c \sin^2 \varphi}{2} \Big\} \Big|_{\varphi_{a,int}}^{\varphi_{a,ext}} + \left\{ \frac{(r_3 - r_2) z_3 \sin \varphi}{2} + \right. \\
 & + \frac{(z_3 + a) (r_{a,ext} - r_3) \sin \varphi}{2} + \frac{a c \sin^2 \varphi}{2} \Big\} \Big|_{\varphi_{a,ext}}^{\pi}
 \end{aligned} \quad (C.8)$$

$$\begin{aligned}
 a_{11,B} = & \left\{ \frac{z_3 (b - r_{nom})^2}{2 (r_3 - r_2)} \ln \frac{1 + \sin \varphi}{\cos \varphi} + \frac{z_3 r_2^2 \sin \varphi}{2 (r_3 - r_2)} - \frac{z_3 (b - r_{nom}) r_2 \varphi}{r_3 - r_2} \right\} \Big|_{\varphi_{2,ext}}^{\varphi_{3,ext}} + \left\{ \frac{z_3 (r_3 - r_2) \sin \varphi}{2} + \right. \\
 & + z_3 (b - r_{nom}) \varphi - z_3 r_3 \sin \varphi + \frac{(z_4 - z_3) (b - r_{nom})^2}{2 (r_4 - r_3)} \ln \frac{1 + \sin \varphi}{\cos \varphi} + \frac{(z_4 - z_3) r_3^2 \sin \varphi}{2 (r_4 - r_3)} + \\
 & - \frac{(z_4 - z_3) (b - r_{nom}) r_3 \varphi}{r_4 - r_3} \Big\} \Big|_{\varphi_{3,ext}}^{\varphi_{a,ext}} + \left\{ \left[\frac{(r_3 - r_2) z_3}{2} + \frac{(z_3 + a) (r_{a,ext} - r_3)}{2} \right] \sin \varphi \right\} \Big|_{\varphi_{a,ext}}^{\pi}
 \end{aligned}$$

$$a_{11} = a_{23} = a_{11,A} - a_{11,B}$$

The term a_{12} is then expressed as follows:

$$\begin{aligned}
 a_{12} = & \left\{ (b - r_{nom}) \varphi - r_2 \sin \varphi + \frac{c \sin^2 \varphi}{2} \right\} \Big|_{\varphi_{2,int}}^{\varphi_{2,ext}} + \left\{ \frac{c \sin^2 \varphi}{2} + (b - r_{nom}) \sqrt{1 + \left(\frac{z_3}{r_3 - r_2} \right)^2} \varphi + \right. \\
 & - r_2 \sqrt{1 + \left(\frac{z_3}{r_3 - r_2} \right)^2} \sin \varphi \left. \right\} \Big|_{\varphi_{2,ext}}^{\varphi_{3,ext}} + \left\{ \frac{c \sin^2 \varphi}{2} + \sqrt{z_3^2 + (r_3 - r_2)^2} \sin \varphi + \right. \\
 & + (b - r_{nom}) \sqrt{1 + \left(\frac{z_4 - z_3}{r_4 - r_3} \right)^2} \varphi - r_3 \sqrt{1 + \left(\frac{z_4 - z_3}{r_4 - r_3} \right)^2} \sin \varphi \left. \right\} \Big|_{\varphi_{3,ext}}^{\varphi_{a,ext}} + \left\{ \frac{c \sin^2 \varphi}{2} + \right. \\
 & + \sqrt{z_3^2 + (r_3 - r_2)^2} \sin \varphi + \sqrt{(r_{a,ext} - r_3)^2 + (a - z_3)^2} \sin \varphi \left. \right\} \Big|_{\varphi_{a,ext}}^{\pi}
 \end{aligned} \tag{C.9}$$

$$a_{12} = a_{24}$$

The third term is presented in the following:

$$\begin{aligned}
 a_{13,A} = & \left\{ \frac{z_3 (b - r_{nom})^2}{2 (r_3 - r_2) \cos \varphi} - \frac{z_3 r_2^2 \cos \varphi}{2 (r_3 - r_2)} + \frac{z_3 c^2 \cos \varphi (\cos^2 \varphi - 3)}{6 (r_3 - r_2)} + \frac{z_3 r_2 (b - r_{nom}) \ln \cos \varphi}{r_3 - r_2} + \right. \\
 & - \frac{z_3 r_2 c}{r_3 - r_2} \left(\frac{\varphi}{2} - \frac{\sin 2\varphi}{4} \right) + \frac{z_3 (b - r_{nom}) c}{r_3 - r_2} \left[\ln \tan \left(\frac{\varphi}{2} + \frac{\pi}{4} \right) - \sin \varphi \right] \left. \right\} \Big|_{\varphi_{2,int}}^{\varphi_{3,int}} + \left\{ - \frac{(r_3 - r_2) z_3 \cos \varphi}{2} + \right. \\
 & - z_3 (b - r_{nom}) \ln \cos \varphi + z_3 r_3 \cos \varphi + c z_3 \left(\frac{\varphi}{2} - \frac{\sin 2\varphi}{4} \right) + \frac{(z_4 - z_3) (b - r_{nom})^2}{2 (r_4 - r_3) \cos \varphi} + \\
 & - \frac{(z_4 - z_3) r_3^2 \cos \varphi}{2 (r_4 - r_3)} + \frac{(z_4 - z_3) c^2 \cos \varphi (\cos^2 \varphi - 3)}{6 (r_4 - r_3)} + \frac{(z_4 - z_3) (b - r_{nom}) r_3 \ln \cos \varphi}{r_4 - r_3} + \\
 & + \frac{(z_4 - z_3) (b - r_{nom}) c}{r_4 - r_3} \left[\ln \tan \left(\frac{\varphi}{2} + \frac{\pi}{4} \right) - \sin \varphi \right] - \frac{r_3 c (z_4 - z_3)}{r_4 - r_3} \left(\frac{\varphi}{2} - \frac{\sin 2\varphi}{4} \right) \left. \right\} \Big|_{\varphi_{3,int}}^{\varphi_{a,int}} + \\
 & + \left\{ - \frac{(r_3 - r_2) z_3 \cos \varphi}{2} - \frac{(z_3 + a) (r_{a,ext} - r_3) \cos \varphi}{2} - a (b - r_{nom}) \ln \cos \varphi + \right. \\
 & + a r_{a,ext} \cos \varphi + a c \left(\frac{\varphi}{2} - \frac{\sin 2\varphi}{4} \right) \left. \right\} \Big|_{\varphi_{a,int}}^{\varphi_{a,ext}} + \left\{ - \frac{(r_3 - r_2) z_3 \cos \varphi}{2} + \right. \\
 & - \frac{(z_3 + a) (r_{a,ext} - r_3) \cos \varphi}{2} + a c \left(\frac{\varphi}{2} - \frac{\sin 2\varphi}{4} \right) \left. \right\} \Big|_{\varphi_{a,ext}}^{\pi}
 \end{aligned} \tag{C.10}$$

$$\begin{aligned}
 a_{13,B} = & \left\{ \frac{z_3 (b - r_{nom})^2}{2 (r_3 - r_2) \cos \varphi} - \frac{z_3 r_2^2 \cos \varphi}{2 (r_3 - r_2)} + \frac{z_3 (b - r_{nom}) r_2 \ln \cos \varphi}{r_3 - r_2} \right\} \Big|_{\varphi_{2,ext}}^{\varphi_{3,ext}} + \left\{ - \frac{z_3 (r_3 - r_2) \cos \varphi}{2} + \right. \\
 & - z_3 (b - r_{nom}) \ln \cos \varphi + z_3 r_3 \cos \varphi + \frac{(z_4 - z_3) (b - r_{nom})^2}{2 (r_4 - r_3) \cos \varphi} - \frac{(z_4 - z_3) r_3^2 \cos \varphi}{2 (r_4 - r_3)} + \\
 & + \frac{(z_4 - z_3) (b - r_{nom}) r_3 \ln \cos \varphi}{r_4 - r_3} \left. \right\} \Big|_{\varphi_{3,ext}}^{\varphi_{a,ext}} + \left\{ - \left[\frac{(r_3 - r_2) z_3}{2} + \frac{(z_3 + a) (r_{a,ext} - r_3)}{2} \right] \cos \varphi \right\} \Big|_{\varphi_{a,ext}}^{\pi}
 \end{aligned}$$

$$a_{13} = a_{21} = a_{13,A} - a_{13,B}$$

The fourth term is then shown:

$$\begin{aligned}
 a_{14} = & \left\{ - (b - r_{nom}) \ln \cos \varphi + r_2 \cos \varphi + c \left(\frac{\varphi}{2} - \frac{\sin 2\varphi}{4} \right) \right\} \Big|_{\varphi_{2,int}}^{\varphi_{2,ext}} + \left\{ c \left(\frac{\varphi}{2} - \frac{\sin 2\varphi}{4} \right) + \right. \\
 & - (b - r_{nom}) \sqrt{1 + \left(\frac{z_3}{r_3 - r_2} \right)^2} \ln \cos \varphi + r_2 \sqrt{1 + \left(\frac{z_3}{r_3 - r_2} \right)^2} \cos \varphi \Big\} \Big|_{\varphi_{2,ext}}^{\varphi_{3,ext}} + \left\{ c \left(\frac{\varphi}{2} - \frac{\sin 2\varphi}{4} \right) + \right. \\
 & - \sqrt{z_3^2 + (r_3 - r_2)^2} \cos \varphi - (b - r_{nom}) \sqrt{1 + \left(\frac{z_4 - z_3}{r_4 - r_3} \right)^2} \ln \cos \varphi + r_3 \sqrt{1 + \left(\frac{z_4 - z_3}{r_4 - r_3} \right)^2} \cos \varphi \Big\} \Big|_{\varphi_{3,ext}}^{\varphi_{a,ext}} + \\
 & + \left\{ c \left(\frac{\varphi}{2} - \frac{\sin 2\varphi}{4} \right) - \sqrt{z_3^2 + (r_3 - r_2)^2} \cos \varphi - \sqrt{(r_{a,ext} - r_3)^2 + (a - z_3)^2} \cos \varphi \right\} \Big|_{\varphi_{a,ext}}^{\pi} \quad (C.11)
 \end{aligned}$$

$$a_{14} = a_{22}$$

The fifth term is reported in the following:

$$\begin{aligned}
 a_{35,A} = & \left\{ \frac{z_3}{2(r_3 - r_2)} \left[(b - r_{nom})^2 \tan \varphi + r_2^2 \varphi + \frac{c^2 \varphi}{2} - \frac{c^2 \sin 2\varphi}{4} - 2r_2(b - r_{nom}) \ln(\tan \varphi + \sec \varphi) + \right. \right. \\
 & \left. \left. - 2(b - r_{nom})c \ln \cos \varphi + 2r_2 c \cos \varphi \right] \right\} \Big|_{\varphi_{2,int}}^{\varphi_{3,int}} + \left\{ \frac{z_3(r_3 - r_2)\varphi}{2} + (b - r_{nom})z_3 \ln(\tan \varphi + \sec \varphi) + \right. \\
 & - r_3 z_3 \varphi - c z_3 \cos \varphi + \frac{z_4 - z_3}{2(r_4 - r_3)} \left[(b - r_{nom})^2 \tan \varphi + r_3^2 \varphi + \frac{c^2}{2} - \frac{c^2 \sin 2\varphi}{4} + \right. \\
 & \left. \left. - 2(b - r_{nom})r_3 \ln(\tan \varphi + \sec \varphi) + 2r_3 c \cos \varphi - 2(b - r_{nom})c \ln \cos \varphi \right] \right\} \Big|_{\varphi_{3,int}}^{\varphi_{a,int}} + \\
 & + \left\{ \frac{(r_3 - r_2)z_3\varphi}{2} + \frac{(z_3 + a)(r_{a,ext} - r_3)\varphi}{2} + a(b - r_{nom}) \ln(\tan \varphi + \sec \varphi) - a r_{a,ext} \varphi + \right. \\
 & \left. - a c \cos \varphi \right\} \Big|_{\varphi_{a,int}}^{\varphi_{a,ext}} + \left\{ \frac{(r_3 - r_2)z_3\varphi}{2} + \frac{(z_3 + a)(r_{a,ext} - r_3)\varphi}{2} - a c \cos \varphi \right\} \Big|_{\varphi_{a,ext}}^{\pi} \quad (C.12)
 \end{aligned}$$

$$\begin{aligned}
 a_{35,B} = & \left\{ \frac{z_3}{2(r_3 - r_2)} \left[(b - r_{nom})^2 \tan \varphi + r_2^2 \varphi - 2r_2(b - r_{nom}) \ln(\tan \varphi + \sec \varphi) \right] \right\} \Big|_{\varphi_{2,ext}}^{\varphi_{3,ext}} + \\
 & + \left\{ \frac{z_3(r_3 - r_2)\varphi}{2} + z_3(b - r_{nom}) \ln(\tan \varphi + \sec \varphi) - r_3 z_3 \varphi + \frac{z_4 - z_3}{2(r_4 - r_3)} \left[(b - r_{nom})^2 \tan \varphi + \right. \right. \\
 & \left. \left. + r_3^2 \varphi - 2(b - r_{nom})r_3 \ln(\tan \varphi + \sec \varphi) \right] \right\} \Big|_{\varphi_{3,ext}}^{\varphi_{a,ext}} + \left\{ \frac{(r_3 - r_2)z_3\varphi}{2} + \frac{(z_3 + a)(r_{a,ext} - r_3)\varphi}{2} \right\} \Big|_{\varphi_{a,ext}}^{\pi}
 \end{aligned}$$

$$a_{35} = a_{35,A} - a_{35,B}$$

The last term is instead equal to:

$$\begin{aligned}
 a_{36} = & \left\{ (b - r_{nom}) \ln(\tan \varphi + \sec \varphi) - r_2 \varphi - c \cos \varphi \right\} \Big|_{\varphi_{2,int}}^{\varphi_{2,ext}} + \left\{ -c \cos \varphi + \right. \\
 & + \sqrt{1 + \left(\frac{z_3}{r_3 - r_2} \right)^2} \left[(b - r_{nom}) \ln(\tan \varphi + \sec \varphi) - r_2 \varphi \right] \Big\} \Big|_{\varphi_{2,ext}}^{\varphi_{3,ext}} + \left\{ -c \cos \varphi + \sqrt{z_3^2 + (r_3 - r_2)^2} \varphi + \right. \\
 & + \sqrt{1 + \left(\frac{z_4 - z_3}{r_4 - r_3} \right)^2} \left[(b - r_{nom}) \ln(\tan \varphi + \sec \varphi) - r_3 \right] \Big\} \Big|_{\varphi_{3,ext}}^{\varphi_{a,ext}} + \left\{ -c \cos \varphi + \sqrt{z_3^2 + (r_3 - r_2)^2} \varphi + \right. \\
 & \left. + \sqrt{(a - z_3)^2 + (r_{a,ext} - r_3)^2} \varphi \right\} \Big|_{\varphi_{a,ext}}^{\pi} \quad (C.13)
 \end{aligned}$$

Acknowledgements

The authors would like to thank MMC Italia Srl (Mitsubishi Materials) for the cutting tools. This work was developed in the *DIGIMAN* project, funded by *Asse 1 Azione 1.2.2 POR-FESR 2014 2020 Emilia-Romagna*.

Declaration of interests

The authors declare that they have no known competing financial interests or personal relationships that could have appeared to influence the work reported in this paper.

CRedit authorship contribution statement

L Bernini: Conceptualization of this study, Methodology, Experimental Tests, Data Analysis, Writing of the paper, Revision of the paper. **P Albertelli:** Conceptualization of this study, Methodology, Experimental Tests, Proof-reading of the paper. **M Monno:** Proof-reading of the paper.

References

- [1] G. Campatelli, A. Scippa, Prediction of milling cutting force coefficients for Aluminum 6082-T4, *Procedia CIRP* 1 (2012) 563–568.
- [2] X. Zhang, T. Yu, Y. Dai, S. Qu, J. Zhao, Energy consumption considering tool wear and optimization of cutting parameters in micro milling process, *International Journal of Mechanical Sciences* 178 (2020) 105628.
- [3] O. Gonzalo, J. Beristain, H. Jauregi, C. Sanz, A method for the identification of the specific force coefficients for mechanistic milling simulation, *International Journal of Machine Tools and Manufacture* 50 (2010) 765–774.
- [4] X. Yuan, S. Wang, X. Mao, H. Liu, Z. Liang, Q. Guo, R. Yan, Forced vibration mechanism and suppression method for thin-walled workpiece milling, *International Journal of Mechanical Sciences* 230 (2022) 107553.
- [5] X.-B. Dang, M. Wan, W.-H. Zhang, Y. Yang, Chatter analysis and mitigation of milling of the pocket-shaped thin-walled workpieces with viscous fluid, *International Journal of Mechanical Sciences* 194 (2021) 106214.
- [6] P. Albertelli, M. Goletti, M. Torta, M. Salehi, M. Monno, Model-based broadband estimation of cutting forces and tool vibration in milling through in-process indirect multiple-sensors measurements, *The International Journal of Advanced Manufacturing Technology* 82 (2016) 779–796.
- [7] M. Wan, W. Yin, W.-H. Zhang, H. Liu, Improved inverse filter for the correction of distorted measured cutting forces, *International Journal of Mechanical Sciences* 120 (2017) 276–285.
- [8] M. Wan, H. Yuan, J. Feng, W.-H. Zhang, W. Yin, Industry-oriented method for measuring the cutting forces based on the deflections of tool shank, *International Journal of Mechanical Sciences* 130 (2017) 315–323.
- [9] D. Wang, L. Penter, A. Hänel, S. Ihlenfeldt, M. Wiercigroch, Stability enhancement and chatter suppression in continuous radial immersion milling, *International Journal of Mechanical Sciences* (2022) 107711.
- [10] K. K. Singh, V. Kartik, R. Singh, Modeling dynamic stability in high-speed micromilling of Ti6Al4V via velocity and chip load dependent cutting coefficients, *International Journal of Machine Tools and Manufacture* 96 (2015) 56–66.
- [11] H. S. Yoon, K. F. Ehmman, Dynamics and stability of micro-cutting operations, *International Journal of Mechanical Sciences* 115–116 (2016) 81–92.
- [12] Y. Altintas, G. Stepan, E. Budak, T. Schmitz, Z. M. Kilic, Chatter Stability of Machining Operations, *Journal of Manufacturing Science and Engineering* 142 (2020) 110801.
- [13] X. Chen, J. Tang, H. Ding, A. Liu, A new geometric model of serrated chip formation in high-speed machining, *Journal of Manufacturing Processes* 62 (2021) 632–645.
- [14] J. Dou, S. Jiao, C. Xu, F. Luo, L. Tang, X. Xu, Unsupervised online prediction of tool wear values using force model coefficients in milling, *The International Journal of Advanced Manufacturing Technology* 109 (2020) 1153–1166.
- [15] D. Liu, Z. Liu, J. Zhao, Q. Song, X. Ren, H. Ma, Tool wear monitoring through online measured cutting force and cutting temperature during face milling Inconel 718, *The International Journal of Advanced Manufacturing Technology* (2022).
- [16] T. Pan, J. Zhang, X. Zhang, W. Zhao, H. Zhang, B. Lu, Milling force coefficients-based tool wear monitoring for variable parameter milling, *The International Journal of Advanced Manufacturing Technology* 120 (2022) 4565–4580.
- [17] M. E. Merchant, Basic Mechanics of the Metal-Cutting Process, *Journal of Applied Mechanics* 11 (1944) A168–A175.
- [18] E. Budak, Analytical models for high performance milling. Part I: Cutting forces, structural deformations and tolerance integrity, *International Journal of Machine Tools and Manufacture* 46 (2006) 1478–1488.
- [19] J.-W. Dang, W.-H. Zhang, Y. Yang, M. Wan, Cutting force modeling for flat end milling including bottom edge cutting effect, *International Journal of Machine Tools and Manufacture* 50 (2010) 986–997.
- [20] Y. Yang, Q. Liu, B. Zhang, Three-dimensional chatter stability prediction of milling based on the linear and exponential cutting force model, *The International Journal of Advanced Manufacturing Technology* 72 (2014) 1175–1185.
- [21] E. Budak, Y. Altintas, E. J. A. Armarego, Prediction of Milling Force Coefficients From Orthogonal Cutting Data, *Journal of Manufacturing Science and Engineering* 118 (1996) 216–224.
- [22] M. Wan, W. H. Zhang, G. Tan, G. H. Qin, New algorithm for calibration of instantaneous cutting-force coefficients and radial run-out parameters in flat end milling, *Proceedings of the Institution of Mechanical Engineers, Part B: Journal of Engineering Manufacture* 221 (2007) 1007–1019. Publisher: IMECHE.
- [23] L. M. Kumanchik, T. L. Schmitz, Improved analytical chip thickness model for milling, *Precision Engineering* 31 (2007) 317–324.
- [24] T. Matsumura, S. Tamura, Cutting force model in milling with cutter runout, *Procedia CIRP* 58 (2017) 566–571.
- [25] Y. Altinta, P. Lee, A General Mechanics and Dynamics Model for Helical End Mills, *CIRP Annals* 45 (1996) 59–64.
- [26] J. Gradiak, M. Kalveram, K. Weinert, Mechanistic identification of specific force coefficients for a general end mill, *International Journal of Machine Tools and Manufacture* 44 (2004) 401–414.
- [27] K. Orra, S. K. Choudhury, Mechanistic modelling for predicting cutting forces in machining considering effect of tool nose radius on chip formation and tool wear land, *International Journal of Mechanical Sciences* 142–143 (2018) 255–268.
- [28] K. Zhu, Y. Zhang, A generic tool wear model and its application to force modeling and wear monitoring in high speed milling, *Mechanical Systems and Signal Processing* 115 (2019) 147–161.
- [29] X. Zhang, T. Yu, P. Xu, J. Zhao, In-process stochastic tool wear identification and its application to the improved cutting force modeling of micro milling, *Mechanical Systems and Signal Processing* 164 (2022) 108233.
- [30] Y. Chen, J. Wang, Q. An, Mechanisms and predictive force models for machining with rake face textured cutting tools under orthogonal cutting conditions, *International Journal of Mechanical Sciences* 195 (2021) 106246.
- [31] K. Kiran, M. C. Kayacan, Cutting force modeling and accurate measurement in milling of flexible workpieces, *Mechanical Systems and Signal Processing* 133 (2019) 106284.
- [32] J. Li, Z. M. Kilic, Y. Altintas, General Cutting Dynamics Model for Five-Axis Ball-End Milling Operations, *Journal of Manufacturing Science and Engineering* 142 (2020) 121003.
- [33] P. Sahoo, T. Pratap, K. Patra, A hybrid modelling approach towards prediction of cutting forces in micro end milling of Ti-6Al-4V titania

- nium alloy, *International Journal of Mechanical Sciences* 150 (2019) 495–509.
- [34] H. Otalora-Ortega, P. Aristimuño Osoro, P. Arrazola Arriola, Uncut chip geometry determination for cutting forces prediction in orthogonal turn-milling operations considering the tool profile and eccentricity, *International Journal of Mechanical Sciences* 198 (2021) 106351.
- [35] Z. Liao, D. Axinte, D. Gao, On modelling of cutting force and temperature in bone milling, *Journal of Materials Processing Technology* 266 (2019) 627–638.
- [36] Y. Srinivasa, M. Shunmugam, Mechanistic model for prediction of cutting forces in micro end-milling and experimental comparison, *International Journal of Machine Tools and Manufacture* 67 (2013) 18–27.
- [37] K. Li, K. Zhu, T. Mei, A generic instantaneous undeformed chip thickness model for the cutting force modeling in micromilling, *International Journal of Machine Tools and Manufacture* 105 (2016) 23–31.
- [38] X. Zhang, K. F. Ehmann, T. Yu, W. Wang, Cutting forces in micro-end-milling processes, *International Journal of Machine Tools and Manufacture* 107 (2016) 21–40.
- [39] H. Li, B. Wu, Development of a hybrid cutting force model for micromilling of brass, *International Journal of Mechanical Sciences* 115–116 (2016) 586–595.
- [40] Y. Zhou, Y. Tian, X. Jing, K. F. Ehmann, A novel instantaneous uncut chip thickness model for mechanistic cutting force model in micro-end-milling, *The International Journal of Advanced Manufacturing Technology* 93 (2017) 2305–2319.
- [41] X. Zhang, T. Yu, W. Wang, Prediction of cutting forces and instantaneous tool deflection in micro end milling by considering tool run-out, *International Journal of Mechanical Sciences* 136 (2018) 124–133.
- [42] X. Jing, R. Lv, Y. Chen, Y. Tian, H. Li, Modelling and experimental analysis of the effects of run out, minimum chip thickness and elastic recovery on the cutting force in micro-end-milling, *International Journal of Mechanical Sciences* 176 (2020) 105540.
- [43] M. Wan, D.-Y. Wen, Y.-C. Ma, W.-H. Zhang, On material separation and cutting force prediction in micro milling through involving the effect of dead metal zone, *International Journal of Machine Tools and Manufacture* 146 (2019) 103452.
- [44] Y. Zhang, S. Li, K. Zhu, Generic instantaneous force modeling and comprehensive real engagement identification in micro-milling, *International Journal of Mechanical Sciences* 176 (2020) 105504.
- [45] L. Zhou, B. Deng, F. Peng, M. Yang, R. Yan, Semi-analytic modelling of cutting forces in micro ball-end milling of NAK80 steel with wear-varying cutting edge and associated nonlinear process characteristics, *International Journal of Mechanical Sciences* 169 (2020) 105343.
- [46] D. Hajdu, A. Astarloa, Z. Dombovari, Cutting force prediction based on a curved uncut chip thickness model, 2021. URL: <http://arxiv.org/abs/2111.00795>, number: arXiv:2111.00795 arXiv:2111.00795 [math].
- [47] Z. Kilic, Y. Altintas, Generalized modelling of cutting tool geometries for unified process simulation, *International Journal of Machine Tools and Manufacture* 104 (2016) 14–25.
- [48] Z. Kilic, Y. Altintas, Generalized mechanics and dynamics of metal cutting operations for unified simulations, *International Journal of Machine Tools and Manufacture* 104 (2016) 1–13.
- [49] M. Nouri, B. K. Fussell, B. L. Ziniti, E. Linder, Real-time tool wear monitoring in milling using a cutting condition independent method, *International Journal of Machine Tools and Manufacture* 89 (2015) 1–13.
- [50] N. Grossi, L. Sallese, A. Scippa, G. Campatelli, Speed-varying cutting force coefficient identification in milling, *Precision Engineering* 42 (2015) 321–334.
- [51] M. Farhadmanesh, K. Ahmadi, Online identification of mechanistic milling force models, *Mechanical Systems and Signal Processing* 149 (2021) 1–18.
- [52] M. Guo, Z. Wei, M. Wang, S. Li, S. Liu, An identification model of cutting force coefficients for five-axis ball-end milling, *International Journal of Advanced Manufacturing Technology* 99 (2018) 937–949.
- [53] Y. Altinta, E. Budak, Analytical Prediction of Stability Lobes in Milling, *CIRP Annals* 44 (1995) 357–362.
- [54] D. Zhan, S. Jiang, J. Niu, Y. Sun, Dynamics modeling and stability analysis of five-axis ball-end milling system with variable pitch tools, *International Journal of Mechanical Sciences* 182 (2020) 105774.
- [55] J. Duplak, M. Hatala, D. Duplakova, J. Steranka, Comprehensive analysis and study of the machinability of a high strength aluminum alloy (EN AW-AlZn5.5MgCu) in the high-feed milling, *Advances in Production Engineering & Management* 13 (2018) 455–465.
- [56] H. Matsuda, H. Sasahara, M. Tsutsumi, Generation of a regularly aligned surface pattern and control of cutter marks array by patch division milling, *International Journal of Machine Tools and Manufacture* 48 (2008) 84–94.
- [57] W. Ji, X. Liu, L. Wang, S. Sun, Experimental evaluation of polycrystalline diamond (PCD) tool geometries at high feed rate in milling of titanium alloy TC11, *The International Journal of Advanced Manufacturing Technology* 77 (2015) 1549–1555.
- [58] V. Gylfen, V. Eidukynas, The Numerical Analysis of Cutting Forces in High Feed Face Milling, Assuming the Milling Tool Geometry, *Procedia CIRP* 46 (2016) 436–439.
- [59] F. Huang, X. Jin, Surface texture generation using high-feed milling with spindle speed modulation, *Precision Engineering* 72 (2021) 13–24.
- [60] P. Zhao, K. Cheng, B. Jiang, L. Zuo, Development of the innovative differential tool wear modeling for high-feed milling and its experimental verification, *Proceedings of the Institution of Mechanical Engineers, Part B: Journal of Engineering Manufacture* 235 (2021) 85–97.
- [61] H. Liu, D. Schraknepper, T. Berge, Investigation of residual stresses and workpiece distortion during high-feed milling of slender stainless steel components, *Procedia CIRP* 108 (2022) 495–500.
- [62] M. A. Rubeo, T. L. Schmitz, Mechanistic force model coefficients: A comparison of linear regression and nonlinear optimization, *Precision Engineering* 45 (2016) 311–321.
- [63] N. Grossi, L. Sallese, A. Scippa, G. Campatelli, Chatter Stability Prediction in Milling Using Speed-varying Cutting Force Coefficients, *Procedia CIRP* 14 (2014) 170–175.
- [64] X. Huang, X. Zhang, H. Mou, X. Zhang, H. Ding, The influence of cryogenic cooling on milling stability, *Journal of Materials Processing Technology* 214 (2014) 3169–3178.
- [65] A. Elefanti, P. Albertelli, M. Strano, M. Monno, Estimation of cutting and friction coefficients in dry and cryogenic milling through experiments and simulations, in: *PROCEEDINGS OF THE 22ND INTERNATIONAL ESAFORM CONFERENCE ON MATERIAL FORMING: ESAFORM 2019*, Vitoria-Gasteiz, Spain, 2019, p. 080006. URL: <http://aip.scitation.org/doi/abs/10.1063/1.5112614>. doi:10.1063/1.5112614.
- [66] E. Tahmasebi, P. Albertelli, T. Lucchini, M. Monno, V. Mussi, CFD and experimental analysis of the coolant flow in cryogenic milling, *International Journal of Machine Tools and Manufacture* 140 (2019) 20–33.
- [67] T. Souflas, H. Bikas, M. Ghassempouri, A. Salmi, E. Atzeni, A. Sabori, I. Brugnetti, A. Valente, F. Mazzucato, P. Stavropoulos, A comparative study of dry and cryogenic milling for Directed Energy Deposited IN718 components: effect on process and part quality, *The International Journal of Advanced Manufacturing Technology* 119 (2022) 745–758.
- [68] P. Albertelli, V. Mussi, M. Monno, Development of generalized tool life model for constant and variable speed turning, *The International Journal of Advanced Manufacturing Technology* 118 (2022) 1885–1901.
- [69] X. Su, X. Yan, C.-L. Tsai, Linear regression, *Wiley Interdisciplinary Reviews: Computational Statistics* 4 (2012) 275–294.
- [70] G. E. P. Box, A GENERAL DISTRIBUTION THEORY FOR A CLASS OF LIKELIHOOD CRITERIA, *Biometrika* 36 (1949) 317–346.
- [71] D. G. Nel, C. A. Van Der Merwe, A solution to the multivariate behrens-fisher problem, *Communications in Statistics - Theory and*

- Methods 15 (1986) 3719–3735.
- [72] J. Tellinghuisen, Statistical error propagation, *Journal of Physical Chemistry A* 105 (2001) 3917–3921.
- [73] D. M. Allen, The Relationship Between Variable Selection and Data Augmentation and a Method for Prediction, *Technometrics* 16 (1974) 125–127.
- [74] T. Tarpey, A Note on the Prediction Sum of Squares Statistic for Restricted Least Squares, *The American Statistician* 54 (2000) 116.
- [75] A. Sauhats, R. Petrichenko, Z. Broka, K. Baltputnis, D. Sobolevskis, ANN-based forecasting of hydropower reservoir inflow, in: 2016 57th International Scientific Conference on Power and Electrical Engineering of Riga Technical University (RTUCON), IEEE, Riga, Latvia, 2016, pp. 1–6. URL: <http://ieeexplore.ieee.org/document/7763129/>. doi:10.1109/RTUCON.2016.7763129.
- [76] A. Botchkarev, Evaluating Performance of Regression Machine Learning Models Using Multiple Error Metrics in Azure Machine Learning Studio, *SSRN Electronic Journal* (2018).
- [77] P. Goodwin, R. Lawton, On the asymmetry of the symmetric MAPE, *International Journal of Forecasting* 15 (1999) 405–408.
- [78] U. Khair, H. Fahmi, S. A. Hakim, R. Rahim, Forecasting Error Calculation with Mean Absolute Deviation and Mean Absolute Percentage Error, *Journal of Physics: Conference Series* 930 (2017) 012002.
- [79] P. Albertelli, V. Mussi, M. Strano, M. Monno, Experimental investigation of the effects of cryogenic cooling on tool life in Ti6Al4V milling, *The International Journal of Advanced Manufacturing Technology* 2021 (2021) 1–13.
- [80] N. A. C. Cressie, H. J. Whitford, How to Use the Two Samplet-Test, *Biometrical Journal* 28 (1986) 131–148.
- [81] C. C. Clogg, E. Petkova, A. Haritou, Statistical Methods for Comparing Regression Coefficients between Models, *American Journal of Sociology* 100 (1995) 1261–1293.